Influence of Low-Level Shear Orientation and Magnitude on the Evolution and Rotation of Idealized Squall Lines. Part I: Storm Morphology and Bulk Updraft/Mesovortex Attributes

MATTHEW C. BROWN,[a] GEOFFREY R. MARION,[a] AND MICHAEL C. CONIGLIO[a]

[a] *National Severe Storms Laboratory, Norman, Oklahoma*

(Manuscript received 17 November 2023, in final form 3 June 2024, accepted 20 June 2024)

ABSTRACT: Observational and modeling efforts have explored the formation and maintenance of mesovortices, which contribute to severe hazards in quasi-linear convective systems (QLCSs). There exists an important interplay between environmental shear and cold-pool-induced circulations which, when balanced, allow for upright QLCS updrafts with maximized lift along storm outflow boundaries. Numerical simulations have primarily tested the sensitivity of squall lines to zonally varying low-level (LL) shear profiles (i.e., purely line-normal, assuming a north–south-oriented system), but observed near-storm environments of mesovortex-producing QLCSs exhibit substantial LL hodograph curvature (i.e., line-parallel shear). Therefore, previous QLCS simulations may fail to capture the full impacts of LL shear variability on mesovortex characteristics. To this end, this study employs an ensemble of idealized QLCS simulations with systematic variations in the orientation and magnitude of the ambient LL shear vector, all while holding 0–3-km line-normal shear constant. This allows for a nuanced examination of how line-parallel shear modulates system structure, as well as mesovortex strength, size, and longevity. Results indicate that hodographs with LL curvature support squall lines with prominent bowing segments and wider, more intense rotating updrafts. Shear orientation also impacts mesovortex characteristics, with curved hodographs favoring cyclonic vortices that are stronger, wider, deeper, and longer-lived than those produced with straight-line wind profiles. These results provide a more complete physical understanding of how LL shear variability influences the generation of rotation in squall lines.

SIGNIFICANCE STATEMENT: Research related to linear storms has largely focused on vertical changes in winds (i.e., shear) oriented perpendicular to squall lines given its ability to balance storm cold pools and keep updrafts upright, thus promoting long-lived storms that presumably can go on to produce rotation. However, squall lines that produce a great deal of rotation often have a component of low-level shear oriented parallel to storms. This study gauges the sensitivity of simulated squall lines to changes in the direction and strength of shear close to the surface. We find that shear oriented parallel to linear storms creates stronger and larger updrafts that in turn support the development of intense and persistent rotation with characteristics supportive of tornadoes. These insights have impacts on both our physical understanding and prediction of the rotation and associated hazards of linear storms.

KEYWORDS: Convective storms/systems; Wind shear; Squall lines; Storm environments; Idealized models

1. Introduction and background

The last five decades of squall-line research have honed in on a number of factors contributing to the strength and longevity of quasi-linear convective systems (QLCSs), perhaps the most significant being vertical wind shear. Early studies (e.g., Hane 1973; Thorpe et al. 1982; Rotunno et al. 1988) noted an important interplay between line-normal (LN) shear over the depth of QLCS cold pools (often 0–2.5/3 km AGL) and outflow buoyancy—each of which generates a forward/rearward acceleration relative to the advancing squall line tied to their magnitude and, in the case of shear, sign (i.e., easterly vs westerly). When these accelerations are imbalanced, attendant QLCS updrafts tilt and weaken in response to downward-directed pressure gradient accelerations and increased entrainment of drier air (e.g., Parker 2010; Peters et al. 2019). This can also be viewed from a vorticity perspective, in which differences in the strength of cold-pool-induced and ambient shear-induced circulations (and associated horizontal vorticity) cause updrafts to tilt either upshear or downshear. When the accelerations (or circulations) balance, however, QLCS updrafts remain upright and strong, with maximized lifting along their nearby outflow boundary (OFB). This balance forms the basis of "Rotunno–Klemp–Weisman (RKW) theory" (Rotunno et al. 1988; Weisman and Rotunno 2004) and has been demonstrated through modeling and observational efforts as one relevant—though insufficient—criterion for long-lived squall lines (Stensrud et al. 2005; Coniglio et al. 2012). More recent work has provided additional context for shear impacts on squall lines. Alfaro and Khairoutdinov (2015) and Alfaro (2017) demonstrated that stronger lower-tropospheric (0–3.5 km AGL) LN shear can modulate the layer-lifting (or broad "slab-like" ascent) associated with squall lines, increasing the fraction of storm-relative inflow

---

Supplemental information related to this paper is available at the Journals Online website: https://doi.org/10.1175/MWR-D-23-0262.s1.

Corresponding author: Matthew C. Brown, matthew.c.brown@noaa.gov

DOI: 10.1175/MWR-D-23-0262.1

that is convectively unstable and reducing midtropospheric buoyancy dilution by entrainment. Similarly, the simulations of Mulholland et al. (2021) showed that increased 0–2.5-km LN shear supports wider and stronger QLCS core updrafts (i.e., stronger updraft pulses embedded within slabular updrafts) that are more resistant to entrainment—again promoting QLCS strength and longevity. These newer additions to the QLCS literature suggest that lower-level shear can support squall-line longevity in a different manner than that described in RKW theory.

The impacts of ambient shear also extend beyond storm maintenance. Squall-line balance and the magnitude of its associated 0–3-km LN shear form two-thirds of the "three ingredients method" (3IM; Schaumann and Przybylinski 2012), a framework commonly used by National Weather Service (NWS) offices and others (e.g., Williams et al. 2018; Murphy et al. 2022) to assess the likelihood for QLCS segments to produce mesovortices and tornadoes. These ingredients include the following:

1) A balanced (or slightly shear dominant) QLCS segment where the gust front, as approximated by the updraft–downdraft convergence zone (UDCZ), is in phase with the leading reflectivity gradient—indicative of upright storm updrafts.
2) 0–3-km line-normal shear magnitude exceeding 30 kt ($\geq$15 m s^{-1}).
3) Local surge or bow in squall line, often associated with rear inflow jet (RIJ; Smull and Houze 1987) formation and intensification.

Observational (Atkins et al. 2004) and modeling studies (Lee and Wilhelmson 2000) reached similar conclusions of Schaumann and Przybylinski (2012), showing that zonal shear values favoring an "optimal balanced state" led to vortex-updraft alignment and strengthening of near-surface rotation. Though this physical framework has shown skill, numerous QLCS mesovortices have been observed despite ambient LN shear below the 3IM threshold above (Ungar and Coniglio 2023). This is not entirely surprising, given the complex interplay of processes that contribute to mesovortexgenesis in squall lines and our limited understanding of how low-level (LL; $\leq$1 km AGL) shear impacts this process.

For supercell thunderstorms, we have a reasonably well-developed conceptual model for how LL shear orientation and magnitude influence updraft forcing, width, rotation, and superposition with near-surface circulation (e.g., Davies-Jones 1984; Wicker 1996; Markowski and Richardson 2014; Coffer and Parker 2015; Peters et al. 2019, 2020; Guarriello et al. 2018; Brown and Nowotarski 2019). For squall lines, however, these physical relationships have yet to be rigorously tested. Most of the seminal idealized studies assessing squall-line mesovortex production do so with straight-line hodographs (i.e., purely LN shear; as in Trapp and Weisman 2003; Weisman and Trapp 2003; Atkins and St. Laurent 2009a,b)—largely due to the implicit assumption that the factors which favor system balance, by extension, favor mesovortexgenesis. In contrast, many studies dealing with (or motivated by) observations of QLCS environments supporting widespread mesovortex and tornado production involve hodographs with substantial LL curvature [i.e., line-parallel (LP) shear; as in Lee and Wilhelmson (1997), Funk et al. (1999), Lyza et al. (2017), and Flournoy and Coniglio (2019)].

Besides worthwhile questions about the relevance of using straight-line hodographs to assess prolific mesovortex production, this inconsistency raises another important question: Should we expect the physical mechanisms contributing to QLCS structure and mesovortexgenesis to look the same across such widely varying LL wind profiles? Add in differences in environmental convective available potential energy (CAPE), interactions with nearby storm structures, spatiotemporal resolution of data, microphysical parameterizations, and other complicating factors across past studies, and it quickly becomes clear why we have yet to reach a consensus on precisely how and why squall lines produce mesovortices.

As such, this study will systematically alter the orientation and magnitude of the LL shear vector and assess their impact on idealized QLCS simulations. A novel hodograph approach—detailed in the proceeding section—will ensure that our squall lines achieve comparable cold pool–shear balance early in storm evolution, allowing for a clear characterization of how varying LL shear attributes subsequently impact the structure, strength, updraft characteristics, and mesovortex production of modeled squall lines. In the present study (Part I), we will focus on QLCS morphology and broader characteristics of its updraft and mesovortex populations. Part II of this study (Brown et al. 2024, manuscript submitted to *Mon. Wea. Rev.*) will delve into the physical processes contributing to these updraft and rotational attributes, via modulations to QLCS propagation and updraft forcing. In total, these papers seek to provide new perspective and clarity for our complicated physical model of QLCS mesovortexgenesis.

2. Methodology

a. Model configuration

The simulations for this study are carried out using Cloud Model 1 (CM1), version 19.10 (Bryan and Fritsch 2002). Horizontal grid spacing is 250 m, with a stretched vertical grid spacing of 125 m below 3 km, increasing to 250-m spacing above 9 km. The model domain is 200 km × 200 km × 20 km. The lateral boundary conditions are periodic in the north–south direction and open radiative in the east–west direction. Subgrid-scale turbulence is parameterized with 1.5-order closure (Deardorff 1980). The NSSL double-moment microphysics scheme of Mansell et al. (2010) is implemented, with default CM1 shape parameters and initial CCN concentration. Additional simulations were performed using Morrison double-moment microphysics (Morrison et al. 2005), but these storms exhibited strong and expansive QLCS cold pools which, while beneficial for system maintenance, appeared to inhibit the generation of long-lived mesovortices. This tendency has been documented in previous sensitivity studies (e.g., Morrison and Milbrandt 2011; Li et al. 2015; Murdzek et al. 2022) and can result in storm cold pools that are incongruous with observed characteristics (e.g., Wade and Parker 2021).

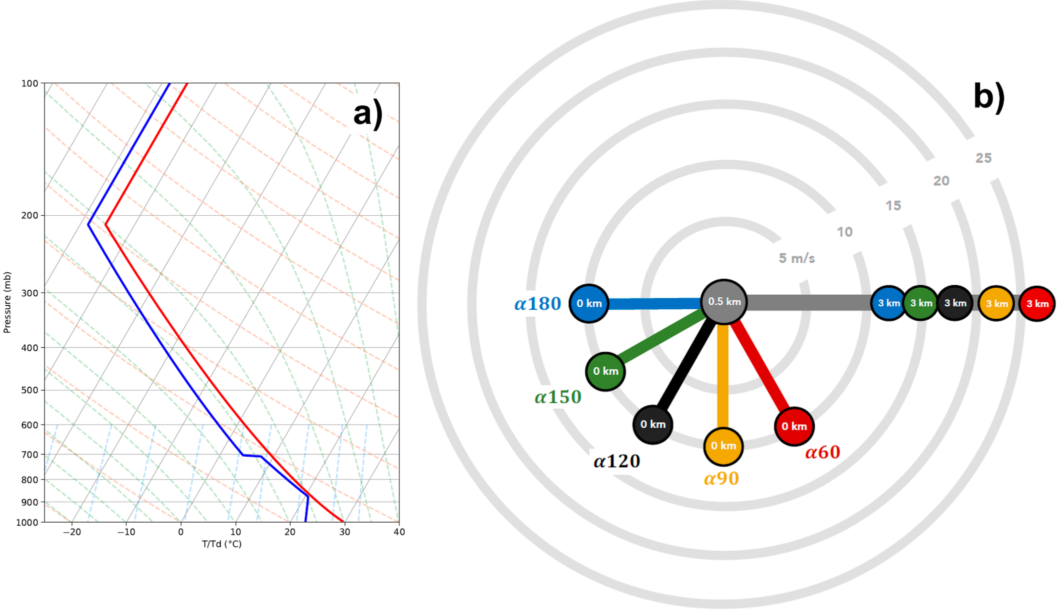

FIG. 1. Schematics of base-state (a) thermodynamic sounding used to initialize squall-line simulations, with temperature (red) and dewpoint temperature (blue) profiles, and (b) hodograph diagram (in u–v space) depicting the range of wind profiles used to initialize simulations, in the case of an LL shear magnitude of 10 m s^{-1}. Each shear vector color responds to a different LL shear orientation with varying angle α and associated 0.5–3-km shear profile above. The profiles are designed such that 0–3-km LN shear is held at a constant value of 22.5 m s^{-1}.

Radiation and surface fluxes of heat, moisture, and momentum are not included in our simulations. Coriolis acceleration is applied to horizontal velocity perturbations,[1] balanced by an imposed large-scale pressure gradient force. The implications of Coriolis forcing for our simulations are discussed in section 4b. The model is seeded with ±0.25-K random θ perturbations throughout its entire horizontal extent within the depth of the cold pool in order to facilitate the development of turbulent structures. Both the upper and lower boundaries are rigid and free slip. Though surface friction has been shown to impact the development of tornadic-like vortices (TLVs) in simulated squall lines (e.g., Schenkman et al. 2012; Xu et al. 2015), concerns persist regarding how best to incorporate drag effects into large eddy simulations (e.g., Markowski and Bryan 2016). Furthermore, the intent of this study is to rigorously assess the impacts of LL shear on simulated squall lines through precise control of hodograph attributes (e.g., LL shear magnitude/orientation, 0–3-km LN shear). Inclusion of frictional effects would induce substantial modifications to the ambient wind profile such that maintaining control of said attributes throughout model integration would be extremely difficult.

b. *Base-state design and initialization*

Simulations are initialized with a horizontally homogeneous base state, comprised of a fixed thermodynamic profile and varying wind profile. The thermodynamic profile, shown in Fig. 1a, is designed after Mulholland et al. (2021), using a Weisman–Klemp analytic profile (Weisman and Klemp 1982) with a surface θ of 302 K. The only difference from this Mulholland et al. (2021) profile is an increase of above-boundary layer relative humidity to 70%, which was chosen to combat entrainment and weakening of midlevel updrafts. The resulting profile contains CAPE of ~2000 J kg^{-1}, a moderate value within the CAPE spectrum for observed squall-line and derecho environments (e.g., Evans and Doswell 2001; Cohen et al. 2007; Thompson et al. 2012).

Wind profiles systematically vary the direction and length of the LL shear vector. Each base-state hodograph—shown schematically in Fig. 1b for an LL shear magnitude of 10 m s^{-1}—is comprised of an LL shear vector extending from the surface to 0.5 km AGL[2] (which we will refer to as our LL shear layer), a zonally varying shear profile from 0.5 to 3 km AGL, and no shear (constant winds) above 3 km. The orientation of the LL shear vector is varied from 60° to 180° clockwise off of horizontal at 30° increments, as depicted by the five different LL shear configurations in Fig. 1b. These shear angles are implemented across three LL shear magnitudes (5, 10, and 15 m s^{-1}), for a total of 15 simulations (Table 1). The key element of our hodograph design is that shear is distributed between the two lowest layers (0–0.5 and 0.5–3 km) such that 0–3-km LN shear is held *constant* at a value of

---

[1] The Coriolis parameter was set to a value of 10^{-4} s^{-1} to match typical midlatitude accelerations.

[2] This shear depth was motivated by the near-storm hodographs of prolific mesovortex-producing squall lines [e.g., those in Atkins et al. (2005) and Flournoy and Coniglio (2019)] showing a substantial LP component below 1 km AGL.

TABLE 1. Simulation names according to their associated LL shear magnitude (m s^{-1}) and orientation as in Fig. 1b.

LL shear magnitude =	5 m s^{-1}	10 m s^{-1}	15 m s^{-1}
α60 (most curved)	α60_m5	α60_m10	α60_m15
α90	α90_m5	α90_m10	α90_m15
α120	α120_m5	α120_m10	α120_m15
α150	α150_m5	α150_m10	α150_m15
α180 (straightest)	α180_m5	α180_m10	α180_m15

22.5 m s^{-1}—which is toward the upper end of the lower-level LN shear values in Cohen et al. (2007) and well above the minimum LN shear threshold for 3IM. Admittedly, this value is more indicative of a highly sheared Southeast/cool-season squall-line environments (e.g., Latimer and Kula 2010; Weiner 2022) but is comparable to the optimal 0–2.5-km LN shear criteria described in Thorpe et al. (1982) and Weisman et al. (1988) and was chosen as it generated long-lived, linear convection.

Following this hodograph design, in the α90_m10 hodograph (golden line/markers in Fig. 1b), for example, base-state surface winds are 10 m s^{-1} from 0° (due northerly), winds at 0.5 km are zero/calm, and winds at 3 km are 22.5 m s^{-1} from 270° (due westerly). Thus, LL shear is purely line parallel, and the entire 22.5 m s^{-1} of LN shear is confined to the 0.5–3-km layer. Conversely, in α180_m10 (blue line/markers in Fig. 1b), there is 10 m s^{-1} of LN shear in the LL shear layer, so only 12.5 m s^{-1} of LN shear is distributed through the 0.5–3-km layer. This hodograph design implies, given sufficiently strong cold pool initiation, that storms forming with these wind profiles will quickly experience the same shear–cold pool balance such that later differences in storm characteristics can be attributed to variations in their LL shear layer. Note that the consequence of our wind profile is variability in the length of the 0.5–3-km shear vector. Though this has ramifications for QLCS propagation (which is explored considerably in Part II), shear in this layer explains $\leq$25% of the variance in the updraft characteristics presented in Part I. Furthermore, the α90 simulations—which have identical 0.5–3-km shear vectors due to their lack of LL line-normal shear—exhibit considerable differences in their storm morphology and updraft characteristics, demonstrating that differences are primarily driven by modulations to our LL shear profile.

Storms are initialized using a cold pool–"dam break" method [similar to the squall-line simulations of Boyer and Dahl (2020), Mulholland et al. (2021), Lovell and Parker (2022), etc.], with maximum potential temperature perturbation of −7 K and a depth of 3.5 km, spanning the entire north–south extent of the model domain. A number of other cold pool intensities and depths were also tested, in tandem with other LN shear depths and magnitudes. The combination listed above was most successful at generating initially balanced squall lines for our given hodograph design that remain linear throughout the entirety of model integration rather than breaking apart into isolated and/or supercell-like structures and support vortexgenesis. Each simulation is integrated for a total of 5 h with a computation time step of 2.5 s, and model output is stored every 5 min.

Storm propagation components are computed iteratively between model time steps. Zonal (u) accelerations are calculated by tracking the domain-averaged x position of storm OFBs—as approximated by the LL-averaged (0–0.5 km) $\theta' = -1$ K contour (similar to Mulholland et al. 2021)—and meridional (v) accelerations are calculated by tracking the change in bowing apex y position (or, in the presence of multiple bows, the average change). Bowing segment identification is detailed in the appendix. If no bowing segments are present, the total v component is set to zero. These accelerations are combined with prescribed model u-move and v-move components to derive a full storm propagation vector, which is subsequently used to compute storm-relative quantities such as storm-relative (SR) flow.

c. Mesovortex identification

Mesovortices are identified using the Okubo–Weiss (OW) parameter (Okubo 1970; Weiss 1991), computed for each model output time. The parameter is used to isolate areas of pure rotation in a flow field and is defined as follows:

$$\mathrm{OW} = \zeta^2 - D^2, \tag{1}$$

where ζ represents vertical vorticity and D is the total deformation field given by

$$D = (D_{\mathrm{shearing}}^2 + D_{\mathrm{stretching}}^2)^{1/2}. \tag{2}$$

OW is defined such that positive values imply a flow field dominated by pure rotation, with larger values corresponding to more strongly rotating objects. Recent studies (e.g., Marion and Trapp 2021; Lovell and Parker 2022) have employed thresholds of $|\mathrm{OW}| \geq 0.01$ s^{-2} (sign dependent on OW definition)—corresponding to $|\zeta| \geq 0.1$ s^{-1} for pure rotation—to identify TLVs in QLCS simulations. Given that we are not specifically interested in TLVs but rather in assessing QLCS updraft and rotational attributes across a broad idealized parameter space, a lower OW bound of 0.005 s^{-2} is selected (resulting in a surface $|\zeta|$ threshold of $\sim$0.07 s^{-1}). Preliminary analysis showed that mesovortex OW tends to decrease rapidly with height. As a result, this rotational threshold is halved above the surface and used to identify vertically contiguous mesovortex layers (similar to vortex depth calculations in Lovell and Parker 2022), allowing us to characterize attributes like mesovortex depth. Other rotational criteria were tested for completeness; the criteria above were found to exclude weak and/or transient vortices while identifying a large enough population of vortices to make robust inferences about their shared characteristics.

A spatiotemporal grouping algorithm is then implemented to track mesovortex objects in both space and time. For the nth mesovortex object at time t ($\mathrm{MV}_{n,t}$), we save its position (x_t, y_t) and sense of rotation (e.g., cyclonic vs anticyclonic). At the next output time $t + 1$, we search with a 5-km radius of (x_t, y_t) for mesovortex objects.[3] Any mesovortices within this radius and with the same sense of rotation as $\mathrm{MV}_{n,t}$ are

---

[3] Note that this methodology works because our simulations utilize domain translation to roughly follow modeled storm structures such that our tracking radius assesses SR motion within modeled squall lines.

isolated, with a match being the vortex that minimizes the distance between $\mathrm{MV}_{n,t}$ and $\mathrm{MV}_{n,t+1}$. Once this match is determined, which constitutes a "mesovortex group," the associated vortices are assigned a unique object identifier and removed from consideration for further matching. The process is iteratively repeated for all vortices at time t, and any unmatched vortices are given their own unique identifier before the process moves to the subsequent model time step. Note that this matching process is prone to error in areas with multiple MVs in close proximity or with complex vortex motion. However, this method proved relatively accurate and tractable for automated analysis of large mesovortex populations. The vortex attributes presented herein represent the mean variable value along the path of each identified mesovortex (i.e., averaged across the vortex objects/time steps associated with each mesovortex group) unless otherwise specified.

3. Results

a. Squall-line morphology

All of the simulations develop long-lived, contiguous squall-line and/or line segments throughout model integration. As intended with the hodograph design, nearly all of these squall lines exhibit upright, balanced updrafts of comparable strength within the first 0.5–1.5 h of model integration (reaching a quasi-steady state by ~1 h). This balance is demonstrated by along-line, OFB-relative updraft and buoyancy composites during this period, shown in Fig. 2, with associated full updraft tilt (in degrees clockwise from vertical). Full updraft tilt is determined by mapping updraft centroids in four layers (0–2.5, 2.5–5, 5–7.5, and 7.5–10 km AGL) and computing the slope of their linear least squares fit line, with $\theta = 0°$ corresponding to a completely upright updraft.

For the m5 and m10 simulations (columns 1–2, respectively, in Fig. 2), early updraft and buoyancy footprints are largely similar in structure and strength, with minimal updraft tilt[4] ($\lesssim 10°$ off vertical in either direction). Additionally, all of the early updrafts are rooted along storm OFBs, except for α150_m15 (Fig. 2l) whose updraft base is displaced eastward ahead of the storm OFB. For higher LL shear values (m10 and m15; columns 2–3, respectively, in Fig. 2), associated QLCS updrafts tilt increasingly rearward (e.g., back over the cold pool) as the hodograph straightens despite having the same prescribed 0–3-km LN shear. Only the α150_m15 and α180_m15 simulations (Figs. 2l,o, respectively) show moderate rearward tilt, with the latter exhibiting a deeper, more negatively buoyant cold pool. However, these updrafts reach their balanced state (with more comparable cold pools) prior to hour 1, perhaps due to the impact of unidirectional shear on precipitation production and transport.

After this initial balanced state, the simulated squall lines diverge in terms of updraft structure and strength, as well as their mesovortex characteristics. The majority of vortexgenesis in our simulations occurs after 2 h. Thus, subsequent analyses will focus on squall-line and mesovortex attributes in the final 3 h of model integration (2–5 h after initialization). To characterize structural differences between the modeled squall lines, LL reflectivity fields are gathered and composited relative to the median OFB position (similar to Fig. 2, but from a plan-view perspective), along with SR inflow direction and strength. There are three general phases of structural evolution in the modeled squall lines: an initial phase (2–3 h) where systems are generally linear, a transitional phase (3–4 h) when internal surges and cusps begin to form, and a mature phase (4–5 h) where bowing segments become fully realized. For the sake of brevity, we focus on the transitional period, but the other time periods will be described. Though not explicitly considered within Part I, QLCS structure evolves rapidly in tandem with large changes in cold pool buoyancy and area and the development of coherent storm downdrafts (or pseudo-RIJs). In our curved hodograph simulations, this downdraft evolution appears crucial for horizontal shearing instability (HSI) release and subsequent vortexgenesis.

Figure 3 shows the resulting reflectivity composites for each simulation, along with LL (0–500 m) averaged SR inflow winds. Comparing across shear orientations, simulations with curved LL shear profiles (α60 and α90; columns 1–2 in Fig. 3, respectively) show kinked squall lines with prominent bowing segments and intense SR inflow with an enhanced meridional (northerly) component. As the LL shear vector is straightened (moving rightward across Fig. 3), associated squall lines become increasingly linear with lowered reflectivity values and weakened, more zonal inflow, deforming into a weak line echo wave-like pattern (LEWP; Nolen 1959) in the α180 simulations. As LL shear magnitude is increased (moving down the rows in Fig. 3), SR flow trends described before become more apparent. Table 2 shows the average area of LL high-reflectivity objects (i.e., greater than 50 dBZ) during hours 2–5. High-reflectivity area increases drastically with increased LL hodograph curvature (up to a 150% increase for m15 simulations), with more subtle increases with increased LL shear magnitude.

These embedded surges persist and become enhanced in the final hour of model integration (not shown), with several squall lines in the m15 simulations consolidating into 1–2 dominant bowing segments, compared to numerous weaker segments in the m5 simulations. If we directly compute bow frequency and length, resulting statistics indicate that as LL shear increases, there is an ~20% decrease in the number of bowing segments present with a corresponding 40% increase in their average length. Nearly all of the simulations show the LL OFB in phase with the leading edge of LL reflectivity, implying some level of "system balance" as per the first component of 3IM. The only simulation which exhibits outflow dominance is α180_m15 (Fig. 3o), potentially indicative of the

---

[4] "Minimal" cold pool/updraft tilt is largely subjective and not clearly defined in the literature. Xu (1992) showed that density currents in the absence of shear attain tilt equal to 60° from horizontal (or $\theta = -30°$ in our framework). Thus, for the purposes of this study, we establish three categories for updraft tilt magnitude—minimal ($|\theta| < 15°$), moderate ($15° \le |\theta| < 45°$), and substantial ($|\theta| > 45°$).

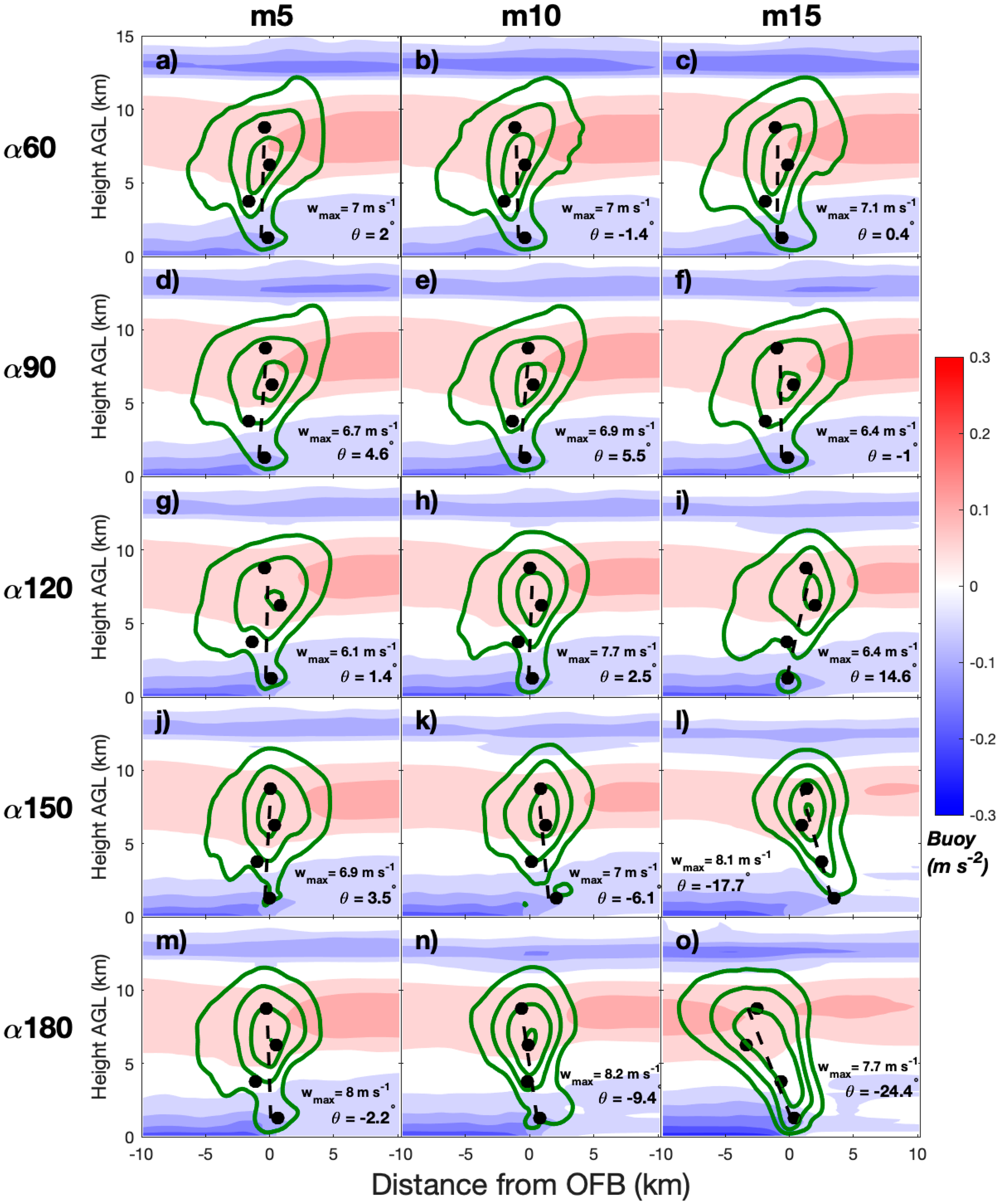

FIG. 2. Composite OFB-relative squall-line cross sections during the period 0.5–1.5 h into model integration, with updraft footprint (green contours; starting at 2 m s^{-1} in 2 m s^{-1} intervals), buoyancy (shaded; m s^{-2}), maximum updraft speed (w_{max}; m s^{-1}), and updraft tilt (θ; in degrees clockwise from upright). The black dots and dashed line represent the updraft centroids and associated best-fit line, respectively, used to approximate updraft tilt. The x-axis units are given as distance from the storm OFB (km).

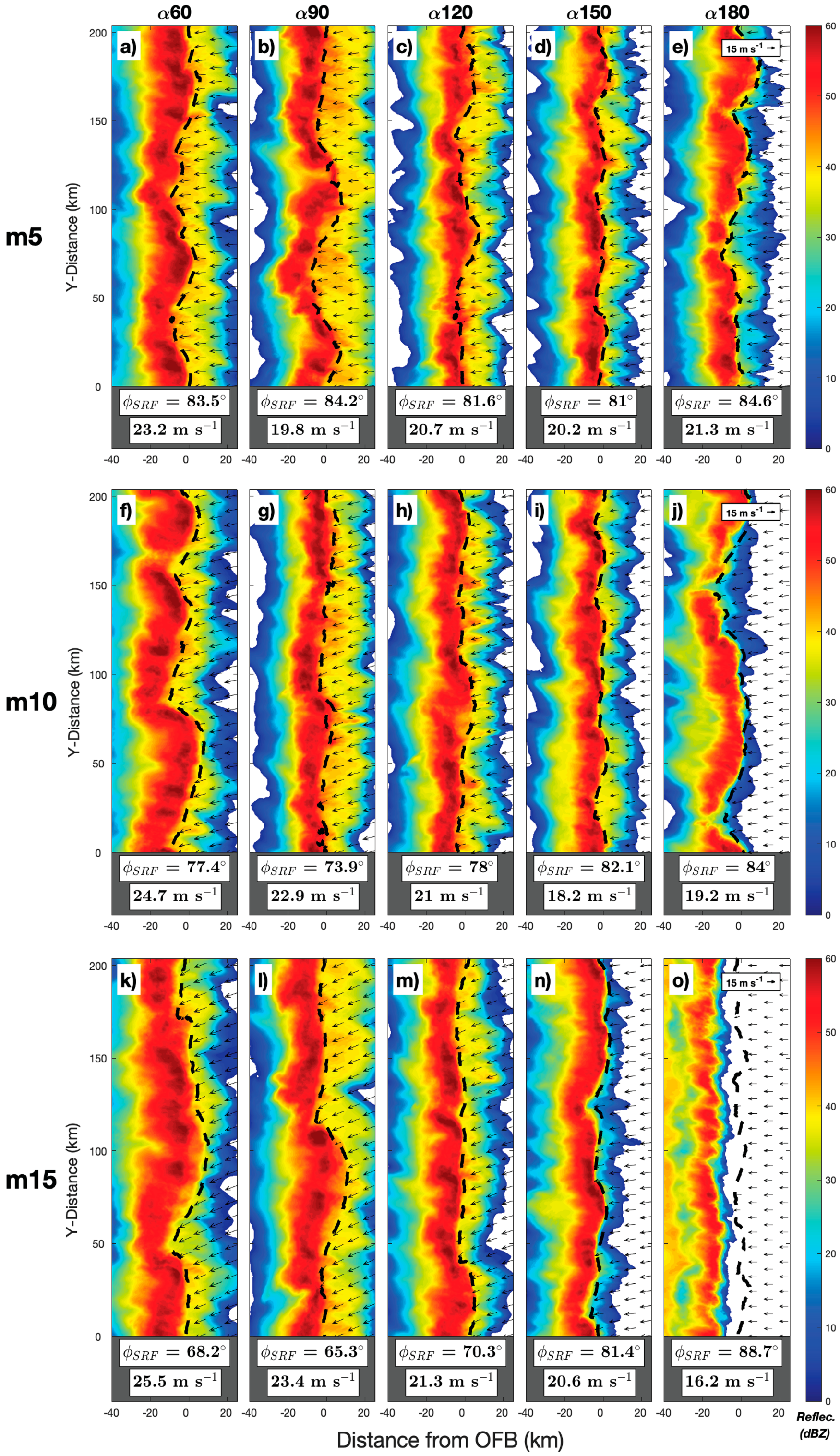

FIG. 3. Composite OFB-relative plan views of LL averaged reflectivity (shaded; dB*Z*) during the hours 3–4 of model integration, with approximate OFB position (dashed black; estimated by the $\theta' = -1$ K contour), LL SR inflow vectors (with a reference vector of 15 m s^{-1}), and average SR flow direction (ϕ_{SRF}; following meteorological wind conventions) and magnitude (m s^{-1}). The *x*-axis units are given as distance from the median storm OFB, and the *y*-axis units are given in N–S distance (both in km).

TABLE 2. Average 2–5-h areal extent ($\times 10^4$ km^2) of LL-averaged reflectivity exceeding 50 dBZ.

	α60	α90	α120	α150	α180
m5	4.09	3.59	2.84	2.61	2.6
m10	4.15	3.13	3.18	2.73	2.41
m15	4.23	3.79	3.33	2.79	1.71

more negatively buoyant cold pools in this simulation that manifest early in model integration (as in Fig. 2o).

b. Updraft strength, structure, and rotation

Next, we consider variations in the QLCS updraft area as a function of shear magnitude and orientation. This is accomplished following the methodology of Mulholland et al. (2021)—in which vertically contiguous slab and core updraft objects are identified using vertical velocity thresholds of 5 and 20 m s^{-1}, respectively. Any objects ≤ 1 km^2 in area (at a given height) are excluded from analysis, and the remaining updraft area profiles are averaged over the 2–5-h period. Figures 4 and 5 show vertical profiles of total and average updraft area (i.e., total updraft area normalized by updraft object counts at each height) as a function of shear orientation and magnitude, respectively, for both the slab and core updraft classifications with accompanying error estimates ($\pm 1\sigma$). A one-sided Welch's t test (Wilks 2011) is used to assess the difference between α60 and α180 (for Fig. 4) or between m5 and m15 (for Fig. 5) area profiles at the 95% confidence level.

As LL curvature is increased, both the total slab and core updraft area (Figs. 4a,b, respectively) similarly increase. Despite moderate overlap, there is statistically significant separation between α60 and α180 updraft area profiles throughout much of the storm depth, which increases if we exclude α180_m15 from our α180 composite (Fig. 1 in the online supplemental material). Similar trends persist when normalizing the updraft area by updraft object counts (Figs. 4c,d) though robust differences are confined to the midlevel core updrafts. The impacts of LL shear orientation on the size of the individual slab (Fig. 4c) and core (Fig. 4d) updraft objects extend well above the prescribed LL shear layer.

Somewhat surprisingly, there is far less separation in profiles when binning by shear magnitude (Fig. 5), with no statistical separation between m5 and m15 profiles (even when excluding α180_m15, as in supplemental Fig. 2). This is not to say that shear magnitude does not play a role—if we break the profiles in Fig. 4 down by shear magnitude (supplemental Fig. 3), updraft area for a given orientation generally scales up with increasing shear magnitude. The key here is that the modulation of QLCS updraft area by LL shear orientation is more dramatic than that of LL shear magnitude.

One pertinent question is whether the presented trends are purely driven by updraft speed, with stronger updrafts manifesting as larger updraft objects given the use of fixed thresholds. Updraft area profiles computed with a vertically varying w (representative w profile applied uniformly across all simulations) and statistically derived thresholds (i.e., 99th percentile w) reveal nearly identical trends across LL shear orientations

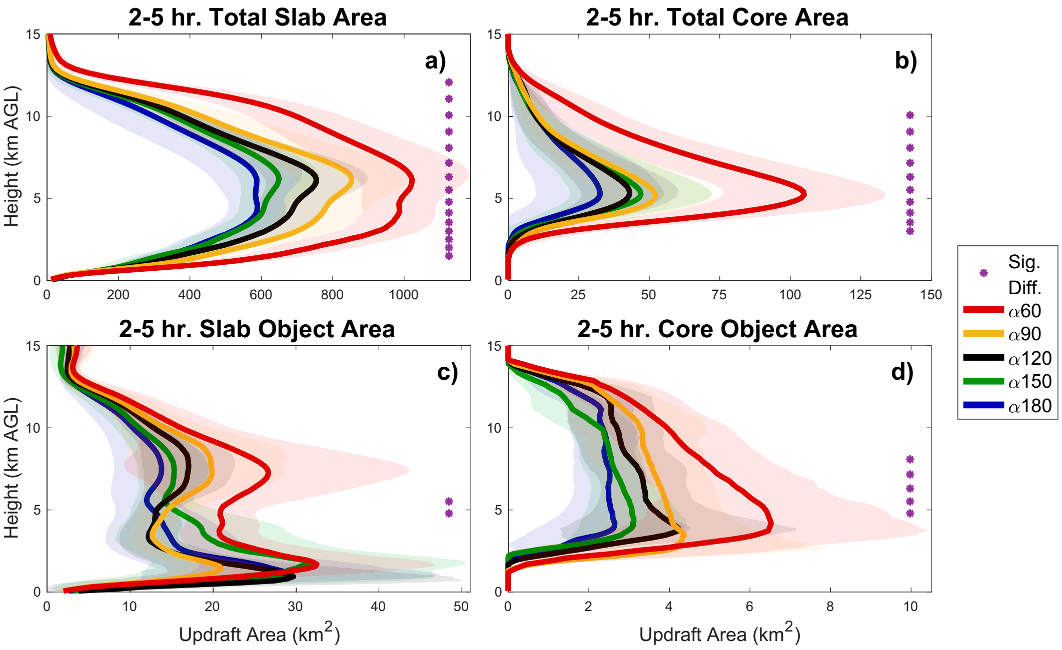

FIG. 4. Vertical profiles of contiguous slab and core updraft area (km^2) for both (a),(b) total and (c),(d) object-averaged, during 2–5 h of model integration. Each color indicates a different LL shear orientation (averaged across shear magnitudes), with solid lines representing the average updraft area profile and associated shading denoting $\pm 1\sigma$. The results of a one-sided Welch's t test (shown in purple asterisks) denote heights at which α60 updraft area exceeds that of α180 (with 95% confidence).

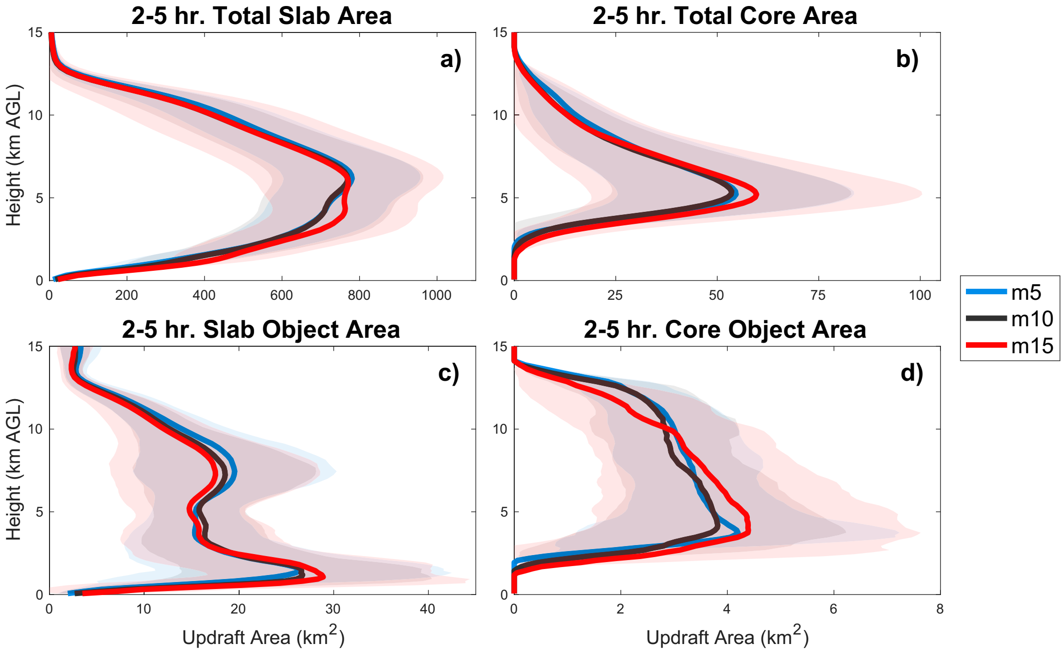

FIG. 5. As in Fig. 4, but broken down by LL shear magnitude (averaged across shear orientations). Welch's *t* test results now compare m5 and m15 updraft area profiles.

and magnitudes (not shown). Additionally, we computed correlations (see supplemental Tables 1 and 2) between profiles of updraft area (supplemental Fig. 3) and maximum vertical velocity ($w_{\max}$; supplemental Fig. 4). This analysis suggested that the overall updraft (and downdraft) footprint somewhat scales by updraft strength (and similarly LL shear magnitude), which meshes with our understanding of convective updraft/downdraft mass flux as in Marion and Trapp (2019). However, the width of individual updraft objects is highly variable and likely driven by other factors. Part II will consider the potential influence that squall-line propagation and associated SR flow may have on updraft attributes.

We also seek to characterize the rotation, if any, of our QLCS updrafts. To this end, we compute OW exceedance frequencies within our contiguous slab/core updraft objects at every model output time, using a threshold of 10^{-4} s^{-2} as in Marion and Trapp (2021) to identify where updrafts are mesocyclonic (i.e., exhibiting pure, cyclonic rotation). We then isolate updrafts that are "persistently rotating" through the 2–5-h period.[5] Note that there is no vertical contiguity requirement for this updraft rotation. Profiles indicating the depth of persistently rotating objects within our slab and core updrafts are shown in Figs. 6 and 7, respectively, along with maximum OW values within this layer ($\mathrm{OW}_{\max}$ in rotating updrafts at each time step) averaged over hours 2–5. Rotation below 2 km AGL is excluded to reduce the signal of ongoing mesovortices.

The depth over which QLCS slab updrafts persistently rotate changes clearly as a function of LL shear orientation (Fig. 6a), with rotation extending lower and through a deeper layer of the atmosphere as LL hodograph curvature is introduced. This trend is also present as we increase LL shear magnitude (Fig. 6b) albeit to a lesser degree. Core updrafts *only* exhibit persistent rotation with curved LL hodographs (Fig. 7a) and/or higher LL shear magnitude (Fig. 7b). As LL shear magnitude is increased for a given shear orientation, a greater portion of core updrafts exhibit rotation (Fig. 7c). When paired with hodograph curvature, increased LL shear fosters core updrafts which contain persistent, cyclonic rotation throughout their entire vertical extent. Deepening of core updraft rotation may be related to the minimum height at which updraft thresholds are met but could also be indicative of dynamic lowering of rotating updrafts within curved hodograph environments [as in Weisman and Klemp (1984)].

In addition to depth of rotation, we also see from corresponding OW maxima that updrafts associated with curved hodographs and/or higher LL shear contain objects exhibiting *stronger* cyclonic rotation, both for slab and core updrafts. Interestingly, the OW values for the slab updrafts are higher than those of core updrafts—likely due to encompassing more rotational objects—which seems somewhat counterintuitive. However, if we were to incorporate information about updraft velocity, as in updraft helicity calculations, the potential for intense vortex stretching would ultimately be higher in

---

[5] Within each slab/core updraft and at every model output time (from 2 to 5 h), we determine the number of grid points exceeding our OW threshold. The median of all these exceedance frequency values (across all simulations and time steps) is calculated within our slab and core updrafts. Updrafts are deemed "persistently rotating" at a given height if their OW exceedance frequency meets or exceeds the median value for at least 80% of the 2–5-h time period (i.e., there is an appreciable population of persistently rotating objects within said updraft).

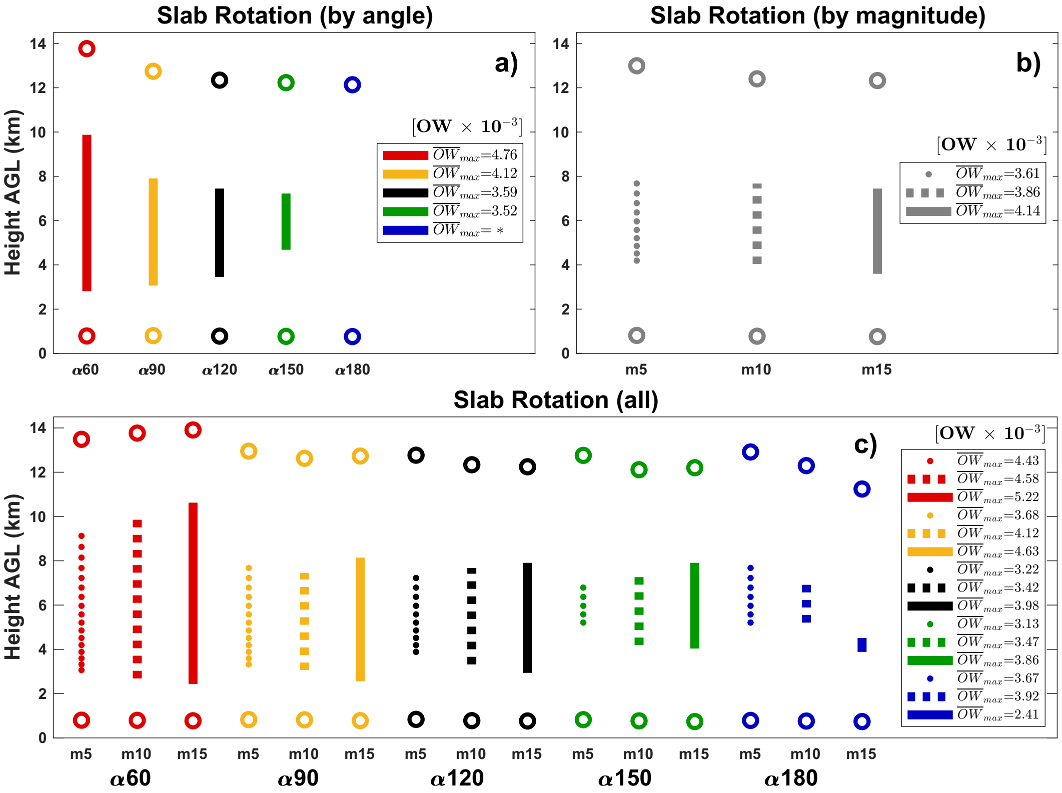

FIG. 6. Vertical profiles of persistent cyclonic rotation within slab updrafts broken down by LL shear (a) orientation, (b) magnitude, and (c) both orientation and magnitude, during the 2–5-h period. The same LL orientation color scheme as in Fig. 4 is used. LL shear magnitude here is denoted by line style—m5 as dotted circles, m10 as dashed squares, and m15 as solid lines. The approximate lower and upper bounds of the QLCS slab updrafts are shown with open circle markers. The average OW maxima ($\times 10^{-3}$ s^{-2}) during this period are displayed in the provided legends for each subset. Asterisks (*) denote simulations which lack persistent rotating updrafts.

core updrafts. Regardless, LL hodograph attributes appear to have considerable influence on the persistence and strength of rotation throughout the entire extent of QLCS updrafts. Additionally, these simulations suggest that persistent midlevel updraft rotation is not an uncommon feature of QLCSs even within the portions exhibiting more “slabular” ascent. Furthermore, the presence of persistent midlevel rotation does not necessarily indicate the presence of embedded supercells, even when collocated with storm updrafts. However, fine-scale observations of squall lines (especially those in environments with extreme hodograph curvature) are needed to determine the exact conditions required to support said rotation and the extent to which this rotation is vertically coherent.

c. Mesovortex production and characteristics

Finally, we assess the production and shared characteristics of mesovortices. First, let us take a cursory look at where intense near-surface rotation is developing within simulated storm structures. Figure 8 shows snapshots of the squall-line segments generating mesovortices that go on to produce the strongest cyclonic vortex (based on near-surface OW) in each simulation. Nearly all of these mesovortices, whose locations are denoted by black stars, form slightly north of or at the apex of localized bowing segments, consistent with observations (e.g., Burgess and Smull 1990; Przybylinski 1995). Rotation maxima tend to coincide with the strongest gradient of near-surface reflectivity as well as the QLCS OFB—albeit with noticeable leading stratiform precipitation in many cases—again consistent with the first component of 3IM. As with Fig. 3, however, α180_m15 is the lone outlier, showing its maximum rotation displaced eastward out in front of the reflectivity gradient along the gust front. There is some indication that the strength of OW maxima-producing cyclonic vortices increases with increased LL hodograph curvature and shear, but distinct trends in mesovortex attributes will be assessed later.

With these insights, we seek to characterize the structure of the updrafts contributing to prolific mesovortexgenesis in our modeled squall lines. To do so, the bowing segment adjacent to “prolific” mesovortex production (e.g., the location of the most and/or the strongest vortices at that time) is subjectively identified for each simulation and time step, and cross sections of relevant variables are collected across their apexes. These

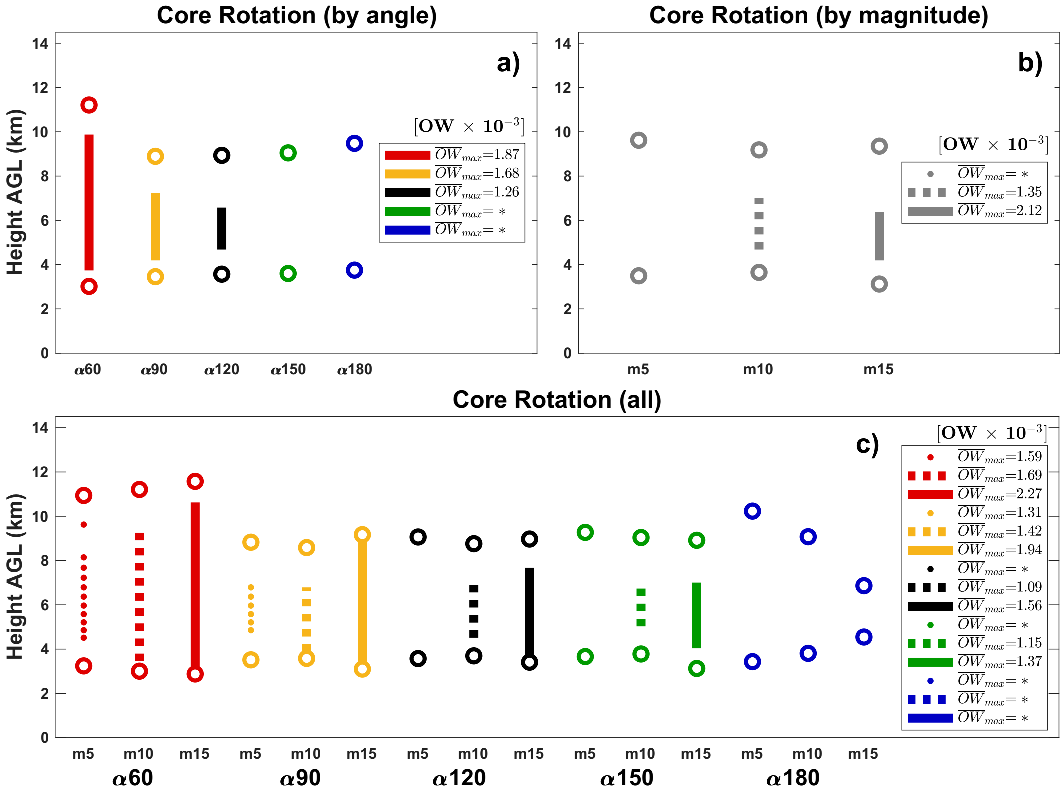

FIG. 7. As in Fig. 6, but for core updrafts.

cross sections, including updraft/downdraft footprints and buoyancy fields, are then composited for hours 2–5, as shown in Fig. 9. Also included is the maximum speed within each average updraft footprint ($w_{\max}$) and tilt (using the same approach as in Fig. 2).

For a given shear magnitude, updrafts are generally stronger in simulations with LL hodograph curvature compared to those with straighter hodographs and have slightly stronger and more spatially coherent downdrafts located closer to their updraft bases (e.g., Fig. 9c vs Fig. 9o). That being said, both α180_m5 and α180_m10 exhibit a slight uptick in updraft strength relative to similar orientation (α120 and α150, for their respective shear magnitudes), perhaps due to differences in cold pool strength. For a given shear orientation, $w_{\max}$ increases monotonically with increasing LL shear magnitude—the exception being α180, largely due to the anomalously tilted, weak updraft in α180_m15 (Fig. 9o). At first glance, there are no discernible trends in updraft tilt in tandem with LL shear orientation or magnitude (or associated $w_{\max}$), with considerable rearward tilt in many cases, at least within the context of mesovortex-producing bowing segments. This matter of system balance and its consequences for vortex production will be addressed later in section 4a.

We also seek to assess the characteristics of the mesovortices themselves—including their frequency, strength, size, and longevity. For each variable, the average value is computed for every mesovortex group (i.e., along each mesovortex path) and aggregated across each individual simulation.[6] The median attributes of the 15 separate mesovortex populations are computed and compared to the median mesovortex characteristics across all simulations (i.e., all shear orientation–magnitude combinations), allowing us to determine whether mesovortex characteristics demonstrably change as a function of LL shear attributes (i.e., whether a given variable is anomalously high or low for a given shear orientation–magnitude combination). These subset median values and deviations from the overall median values are summarized in polar plots, as shown in Figs. 10–12, with each polar segment corresponding to a different shear orientation–magnitude combination (following Fig. 1b).

Starting with mesovortex count (Fig. 10a), we see that the greatest mesovortex production generally occurs in the most curved LL shear profiles, while more zonal shear profiles have comparatively reduced production. The sole exception is the α180_m15 simulation, which produces more mesovortices than any of our simulations, but results later in this section will show that these vortices differ from those produced in α60/α90. Across all shear orientations, there are consistent increases in mesovortex production with increasing LL shear

---

[6] For vertically dependent properties like depth and width, the maximum variable value over the depth of each mesovortex object is computed before being averaged in time.

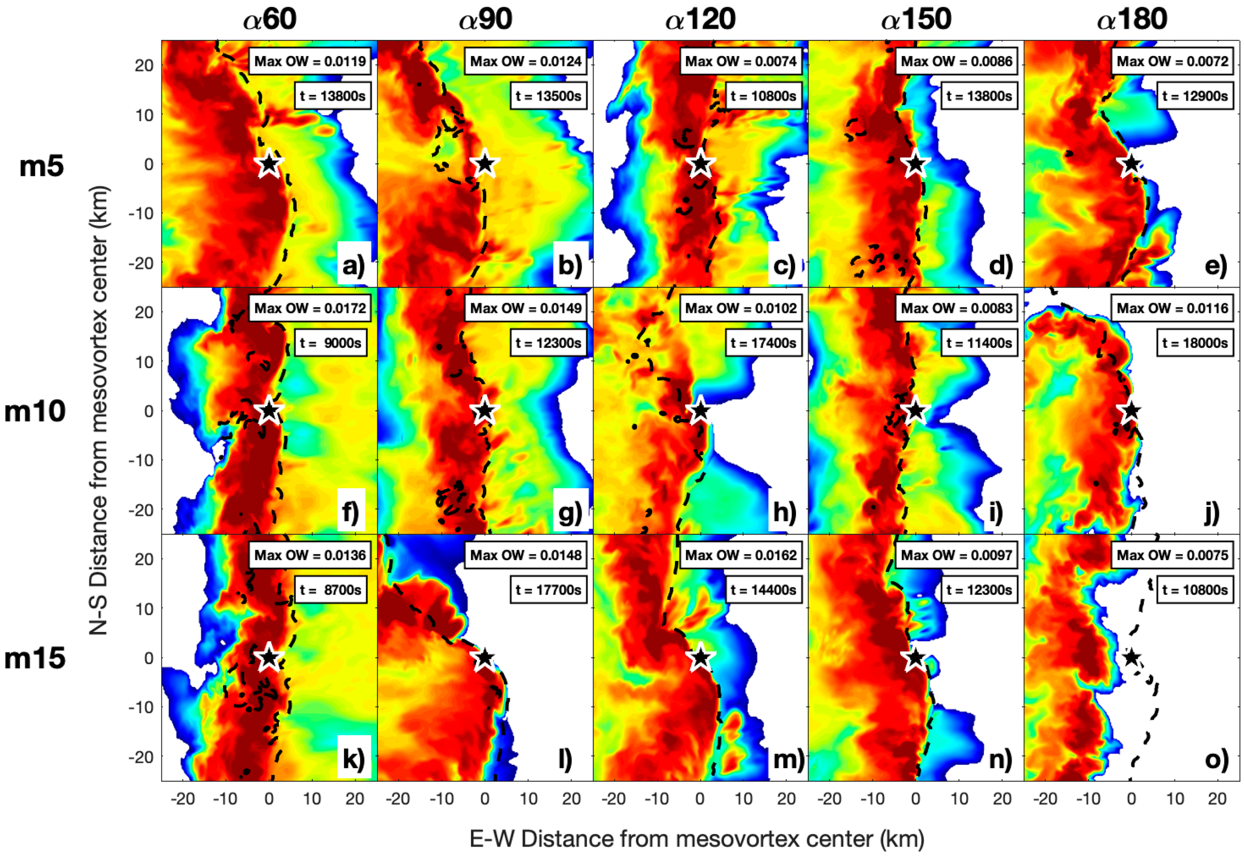

FIG. 8. Snapshots of QLCS segments at the time of vortexgenesis for the vortices which go on to produce maximum OW (associated with cyclonic rotation) in each simulation. The approximate OFB position is shown, as in Fig. 3, along with the subsequent surface OW maxima (s^{-2}) and genesis time (in seconds into model integration). The black star denotes the center of each analyzed mesovortex.

magnitude, particularly as we step up from 5 to 10 m s^{-1}. If we limit these counts to cyclonic rotation (Fig. 10b), we see that most of these trends are driven by changes in populations of cyclonic mesovortices. Combining the information in Figs. 10a and 10b, we consider the fraction of all mesovortices associated with cyclonic rotation (Fig. 10c). More curved LL shear orientations—particularly α90 and α120—correspond to predominantly cyclonic mesovortices. As the LL shear vector straightens, cyclonic vortices become less prevalent (or alternatively, anticyclonic vortices are more prevalent), with α180_m15 containing nearly an equal proportion of cyclonic and anticyclonic mesovortices. Unlike mesovortex count, the proportion of cyclonic vortices does not appear to vary uniformly by shear magnitude. If we increase our rotational threshold for mesovortex identification [as in the TLV identification of Marion and Trapp (2021)], sample size understandably decreases, but the same trends in vortex production and sign persist with only our curved hodographs producing strong, persistent cyclonic vortices (not shown).

The polar diagrams for mesovortex strength are shown in Fig. 11. To make more robust inferences about perceived differences between mesovortex populations, we consider the statistical significance of differences between low-shear (LS; m5 simulations) and high-shear (HS; m15 simulations) mesovortex populations, as well as between those in the more curved (α60/α90) and more straight-line (α150/α180) simulations. Given noticeable skew in several variable distributions, statistical significance is assessed using a one-sided Wilcoxon rank-sum test (Wilks 2011) to assess if population 1 (e.g., high-shear or curved hodographs) has a higher median variable value than population 2 (e.g., low shear or straight hodographs). We also perform an additional set of tests in which the α180_m15 simulation is excluded, given the unique nature of its associated mesovortices, as evidenced by Fig. 10 and subsequent polar plots. The results of those tests as they relate to rotational strength are summarized in Table 3. Comparing our HS and LS populations, we see that HS mesovortices exhibit higher OW, and this increased rotation is statistically significant. This is even more apparent for the mesovortices produced in our curved hodograph simulations (Figs. 11a,b). Looking closer, though, we see that these increases are driven primarily by a strengthening of cyclonic vortices (Fig. 11b), whereas the strength of anticyclonic mesovortices lacks a coherent pattern (Fig. 11c).

Figure 12 and Table 4 show similar polar plots and statistics, respectively, regarding mesovortex size and timing. Median mesovortex persistence is heavily influenced by a large population of short-lived vortices in α180_m15, so the 90th

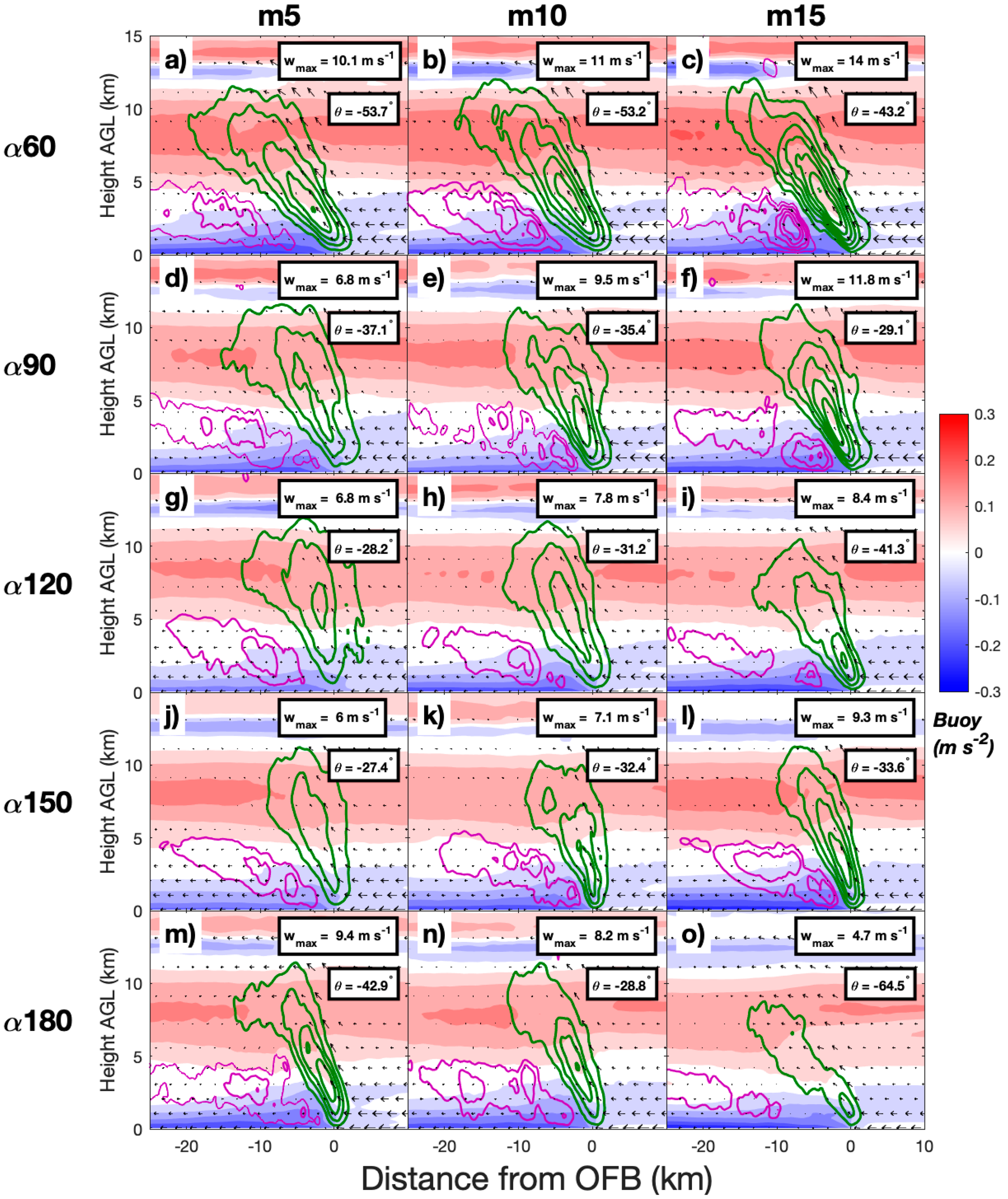

FIG. 9. Composite OFB-relative cross sections across simulated squall lines (adjacent to mesovortex formation) during hours 2–5, with updraft footprint (green contours; starting at 2 m s^{-1} in 2 m s^{-1} intervals), downdraft footprint (purple contours; starting at −0.5 m s^{-1} in 0.5 m s^{-1} intervals), buoyancy (shaded; m s^{-2}), SR zonal winds (quivered), maximum updraft speed (w_{max}; m s^{-1}), and full updraft tilt (θ; in degrees clockwise from upright). The x-axis units and reference wind vector are the same as in Figs. 2 and 3, respectively.

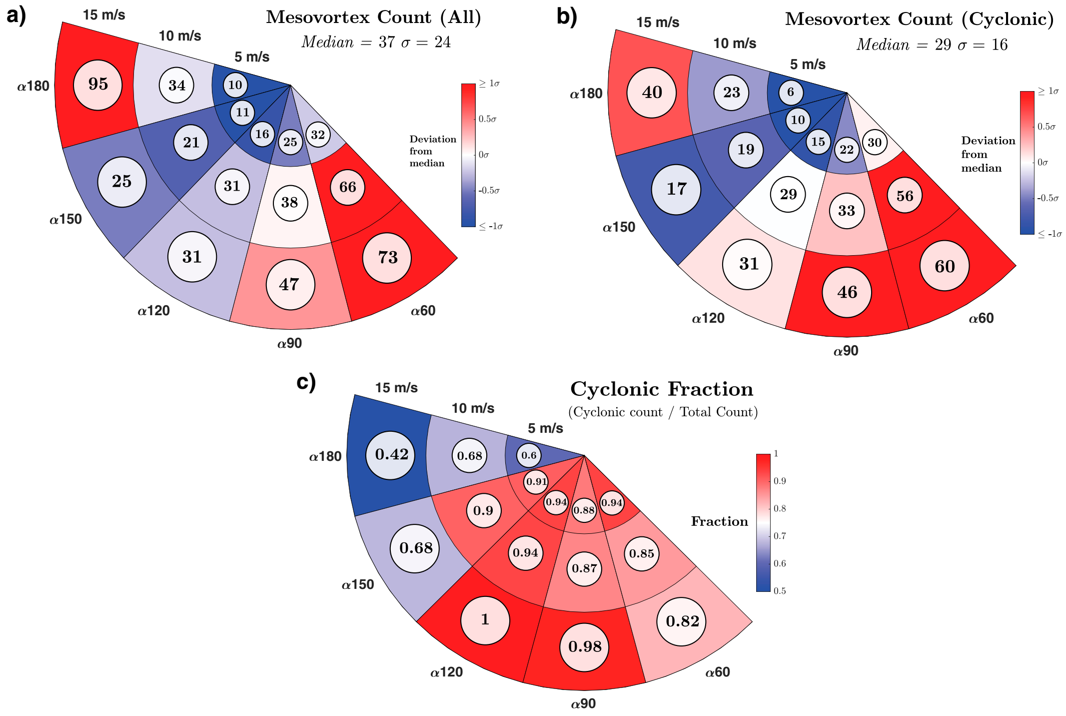

FIG. 10. Polar plots of (a) total mesovortex counts, (b) cyclonic mesovortex counts, and (c) cyclonic mesovortex fraction (cyclonic counts normalized by total counts), broken down by LL shear orientation and magnitude (following the hodograph design of Fig. 1b). The variable values are displayed in the circle within each orientation–magnitude polar slice. In (a) and (b), the shading represents the deviation of the subset median (i.e., the median variable value in each LL orientation–magnitude combination) from the population median (i.e., median across all combinations). In (c), the actual fraction itself is used for shading.

percentile is used for Fig. 12c. Despite the apparent trends in Figs. 12a and 12b, the corresponding statistical tests indicate that the amount of LL shear present does not appear to impact mesovortex size. Unsurprisingly, this is largely related to the inclusion of abnormally narrow and shallow α180_m15 vortices (Figs. 12a,b). When α180_m15 is excluded, there is a robust relationship between increased shear and wider, deeper mesovortices. HS mesovortices also form earlier in our simulations (compared to LS simulations) and persist slightly longer (Figs. 12c,d). The same relationships generally hold true comparing our curved and straight-line simulations, with curved LL shear profiles supporting wider and deeper mesovortices—except their vortices occur *later* in simulations. Unlike the HS versus LS comparison, however, this is more an indication of prolonged mesovortexgenesis than a distinct shift in timing. If we solely consider the size and timing of cyclonic vortices (Table 5), several of the same trends exist. Additionally, robust relationships come out between increased shear and larger cyclonic vortices, as well as the presence of longer-lived cyclonic mesovortices with curved hodographs (even when excluding α180_m15), consistent with the findings of Marion and Trapp (2021).

Considering both the α180_m15 results themselves and the impact of their exclusion on the aforementioned statistics, we see how anomalous the characteristics of their mesovortices are relative to other simulations. Despite prolific vortex production (Figs. 10a,b), the mesovortices in α180_m15 are noticeably shallower and smaller than other high-shear simulations (Figs. 12a,b)—possibly attributable to its shallower, weaker, and tilted updrafts (Figs. 3o and 9o). The processes contributing to mesovortex formation and their properties will be addressed in greater detail in Part II of this study.

4. Discussion and conclusions

a. *QLCS structure and balance*

Within the scope of RKW theory, 3IM, and other related studies (e.g., Atkins et al. 2005), we expect that the most intense squall lines are those with upright and/or "balanced" updrafts, which would in turn support prolific mesovortexgenesis. To assess this matter within our simulations, we consider the distribution of system balance-related parameters in the mesovortex-producing (MV) segments that make up our Fig. 9 composites. These parameters include full updraft tilt, lower updraft tilt (same centroid-based process but computed over the 0–2 km layer), 0–3-km LN shear, and UDCZ-to-reflectivity (UDCZ-to-R) distance (as in first component of 3IM and Ungar and Coniglio 2023). Details of 3IM calculations are summarized in the provided appendix. Note that we are now considering segmentwise LN shear (i.e., accounting for local OFB geometry), as opposed to systemwide LN

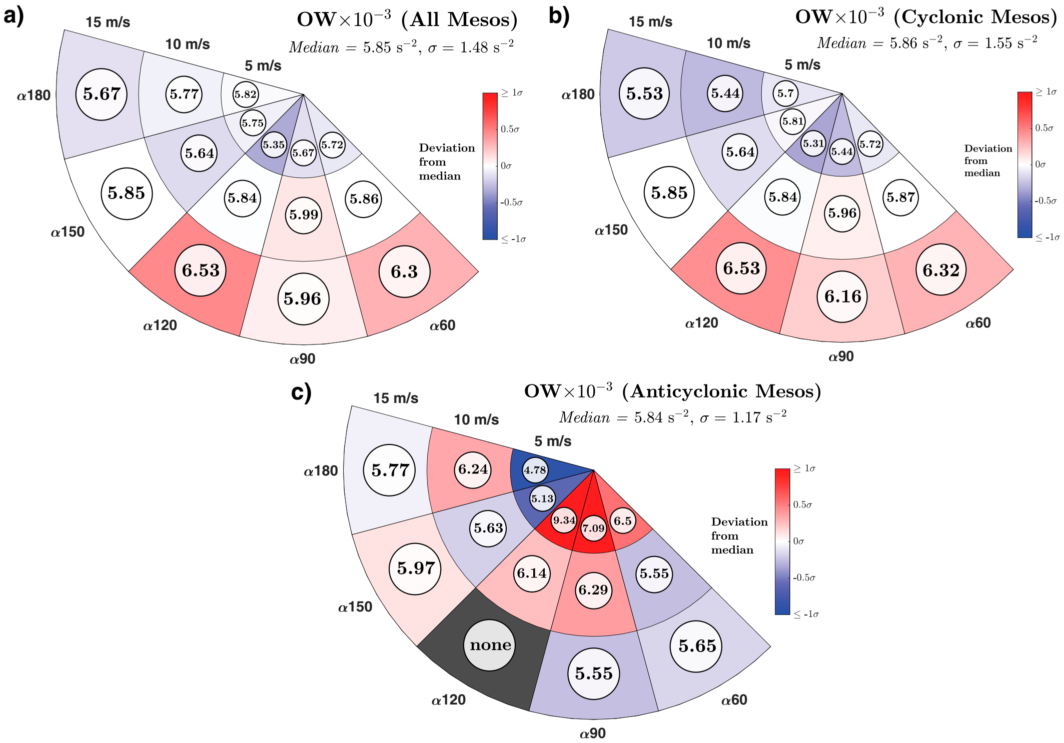

FIG. 11. As in Fig. 10, but for mesovortex surface OW (×10^{-3} s^{-2}) for (a) all, (b) cyclonic, and (c) anticyclonic vortices.

shear prescribed by our hodograph design. Segments void of mesovortex production (non-MV) are randomly selected at each output time to build null populations for comparison.

Violin plots of balance metrics in MV and non-MV segments are shown in Fig. 13. Full updraft tilt (row 1) lacks a clear trend as a function of LL shear orientation, while lower updraft tilt (row 2) shows slightly more upright updrafts as the LL hodograph straightens. However, both metrics indicate moderate-to-extreme rearward (upshear) tilt, whose values do not vary clearly with associated 0–3-km LN shear (row 3). This, combined with the fact that both MV and non-MV populations exhibit noticeable spread in their updraft tilt, indicates that mesovortex formation (or the lack thereof) can occur across a broad spectrum of updraft angles—even those indicating considerable rearward tilt.

Many of the MV segments correspond with "suboptimal" shear in accordance with 3IM, similar to the findings of Ungar and Coniglio (2023). Note that when we move to a segmentwise perspective, shear values are noticeably lower (compared to base state shear) due to the prevalence of local bowing segments near mesovortexgenesis. The majority of segments, both MV and non-MV, also show minimal UDCZ-to-*R* distance (again consistent with Ungar and Coniglio 2023), except for the high values associated with outflow dominance seen in some α180 storms (e.g., Figs. 3 and 8o). Most important, however, is that almost *none* of the balance metrics show appreciable separation between their MV and non-MV populations. The only hints of separation are increased LN shear for α60/α90 MV segments in comparison with their respective non-MV segments. This separation increases slightly if we incorporate information about UDCZ-to-*R* distance and bowing segments (i.e., into a total, 3IM-motivated metric) but only for curved hodograph simulations (not shown). Regardless, many segments that satisfied 3IM—indicative of system balance (and upright updrafts by RKW theory)—still exhibited considerably rearward tilted updrafts. It is possible that once local surges or bows form, updraft tilt increases locally, but not in a way that inhibits ongoing mesovortex formation or is detrimental to overall system longevity. Put simply, it is not evident within these simulations whether system balance is a controlling factor for mesovortexgenesis within QLCS segments.

In refining the simulations at hand, a number of different cold pool strength and environmental LN shear values were tested. In general, attaining cold pool–shear balance was vitally important for the maintenance and persistence of linear convective features beyond the first 1–2 h of model integration, particularly in high-shear regimes. Mesovortex formation, however, appeared to be more sensitive to other model parameters, including the vertical distribution of shear, Coriolis forcing, and microphysical attributes. Granted, even with these sensitivity simulations, we are only testing a portion of the broader CAPE–shear parameter space in which squall lines and their associated rotation occur. Even so, this again calls into question the role that squall-line balance plays in mesovortex formation and maintenance. Given at least marginal balance (e.g., in the range of the upshear-tilted updrafts of ~20° to 50°, as shown in Figs. 9 and 13), robust updraft

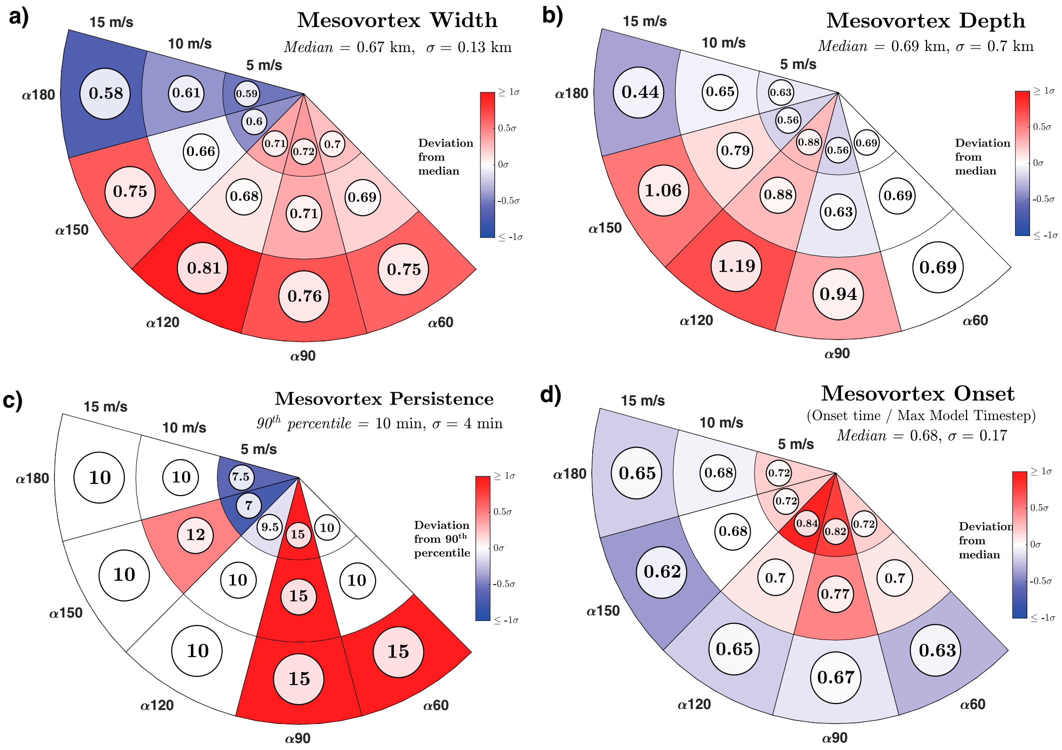

FIG. 12. As in Fig. 10, but for mesovortex (a) width (km), (b) depth (km), (c) persistence (min), and (d) onset fraction (fractional time into simulation that mesovortices form). The 90th percentile is used for mesovortex persistence, in order to account for the population of short-lived vortices in α180_m15 that skew the overall median persistence.

development and mesovortexgenesis can still take place, suggesting that these processes are more influenced by other internal and external processes than those that control updraft tilt.

b. *Mesovortex attributes*

One of the more intriguing results of the mesovortex analysis presented earlier is the dominance of cyclonic vortexgenesis in our curved hodograph simulations and, conversely, increased anticyclonic vortexgenesis in straight-line hodograph simulations (Fig. 10c). These vortex characteristics suggest that the development of squall-line rotation depends, at least in part, on their near-storm LL shear profiles—particularly their LL line-parallel shear. In a recent observational analysis of 50 cyclonic mesovortex-producing QLCSs, Ungar and Coniglio (2023) find that all cases exhibit at least ~5 m s^{-1} of 0–1-km LP shear. Coincidentally, the second conclusion of Lee and Wilhelmson (2000) reads as follows:

> A threshold likely exists between 5 and 10 m s^{-1} of velocity change across the convergence boundary of the line-parallel wind, below which, the [cyclonic mesovortexgenesis] potential is minimal, and above which, the boundary is viable as [a cyclonic mesovortexgenesis] site …

Though the cyclonic mesovortexgenesis in the simulations of Lee and Wilhelmson (2000) develops specifically through the release of HSI, this LP shear range is consistent with the broader cyclonic mesovortex conclusions of Ungar and Coniglio (2023), suggesting that the physical implications of their statement extend beyond its original intent. It is important to note that both the Lee and Wilhelmson (2000) study and 3IM center around the formation (or lack thereof) of QLCS tornadoes, whereas this study is more focused on the

TABLE 3. *P* values associated with one-sided Wilcoxon rank-sum tests comparing mesovortex maximum surface OW (path-averaged) in HS and LS, as well as curved (α60/α90) and straight (α150/α180) hodograph vortex populations—broken down for all, cyclonic (C) and anticyclonic (AC) vortices. Bolded values indicate population differences that are significant at the 95% confidence level. Asterisks indicate test values that are significant when the α180_m15 simulation is excluded.

	Sfc OW$_{max}$ (all)	Sfc OW$_{max}$ (C)	Sfc OW$_{max}$ (AC)
HS > LS	**0.0022***	**0.0113***	0.4102
HS ≤ LS	0.9978	0.9887	0.5898
Curved > straight	**0.0001***	**0.0001***	0.1863
Curved ≤ straight	0.9999	0.9999	0.8137

TABLE 4. As in Table 3, but for path-averaged maximum mesovortex width and depth, as well as vortex onset time and persistence.

All vortices	Max width	Max depth	Onset time	Persistence
HS > LS	0.5241*	0.6923*	0.9999	**0.0329***
HS ≤ LS	0.4759	0.3077	**0.0001***	0.9671
Curved > straight	$\mathbf{1.48 \times 10^{-4}}$*	$\mathbf{1.72 \times 10^{-5}}$	**0.0245**	0.0579
Curved ≤ straight	~1	~1	0.9755	0.9421

propensity for strong and/or long-lived cyclonic vortices. The development of QLCS tornadoes (or any tornadoes, for that matter), particularly those arising from HSI release, primarily coincides with intense cyclonic rotation. Therefore, while different in their intent, the physical implications of this study are inextricably linked to past work.

In any case, if we categorize LP shear owing to our base-state LL orientation-shear parameter space, as in Fig. 14, we see that both hodograph curvature and moderate/high LL shear are required to meet the LP shear criteria outlined in these studies. Comparing Fig. 14 to the earlier mesovortex polar plots (Figs. 10–12), we see this LP shear distribution resembles that of cyclonic mesovortex fraction (Fig. 10c) and, more impressively, is nearly *identical* to our cyclonic mesovortex strength polar plot (Fig. 11b). Though speculative, this similarity strongly implies a physical linkage between LP shear and cyclonic rotation. We reiterate that this is not to say that the existence of LP shear is a requirement for vortexgenesis or even cyclonic vortexgenesis—our α180 simulations all produce cyclonic rotation. Rather, LP shear appears to be a crucial contributor to the development of *intense and long-lived* cyclonic vortices—the dynamic linkages of which motivate Part II.

A secondary, though critical, factor is the role of Coriolis forcing. Sensitivity tests varying the inclusion and strength of Coriolis accelerations demonstrated that Coriolis forcing led to the weakening (or complete extinction) of anticyclonic vortices, particularly those which are initially more weak and transient. This result is consistent with the convergence of planetary vorticity, as described in Trapp and Weisman (2003) and Weisman and Trapp (2003), and explains why some of our straight-line simulations still bear a preference toward cyclonic rotation (as in Fig. 10c). All of this being said, the dominance of cyclonic-only vortices with increased LL hodograph curvature was a *consistent* and robust result regardless of system sensitivities resulting from test simulations with varied initiation techniques, microphysical schemes, Coriolis forcing, LL shear orientations/magnitudes, midlevel RH, etc.

One last physical consideration is the propensity of storms in environments with increased LL shear and curvature to acquire or develop rotation via supercell-like processes. Indeed, there is the potential for strongly curved hodographs to support the development of right-moving supercells embedded within (or interacting with) broader linear structures, which would inherently favor the development of cyclonic rotation. Careful consideration was given during the development of these simulations to maintain continuous reflectivity fields and avoid supercellular behavior (e.g., archetypal flow/reflectivity features and single dominant mesocyclones)—increasing confidence that embedded supercell structures are not present in the modeled storms. Furthermore, the updraft width and rotation trends presented apply to both slab and core updrafts rather than to only core updrafts, as one might expect for embedded supercell features. As such, it is apparent that the aforementioned studies and the results presented herein tell a similar story—LP shear plays a crucial role in the development of strong and persistent cyclonic mesovortices in squall lines.

c. *Summary and future work*

In this study, we have systematically varied both the direction and magnitude of low-level (0–0.5 km) shear while maintaining constant 0–3-km LN shear and assessed its impact on the evolution, updraft characteristics, and mesovortexgenesis of initially balanced, comparable squall lines. In doing so, we have reached the following primary conclusions:

1) LL hodograph curvature supports squall lines that develop intense bowing segments with larger embedded high-reflectivity features, while straight-line hodographs result in weaker squall lines with weaker and more diffuse bowing segments.
2) QLCS updrafts (both slab and core) in curved hodograph environments are stronger and wider and exhibit deeper and more intense rotation than those realized in straight-line hodographs. These relationships are strengthened when paired with increased LL shear magnitude.
3) LL hodograph curvature supports stronger, wider, deeper, and more persistent mesovortices, particularly those exhibiting cyclonic rotation. Increasing LL shear magnitude (for a given LL shear orientation) also tends to increase mesovortex production.

TABLE 5. As in Table 4, but for cyclonic-only mesovortices.

Cyclonic only	Max width	Max depth	Onset time	Persistence
HS > LS	0.0872*	**0.0255***	0.9961	0.0897*
HS ≤ LS	0.9123	0.9745	**0.0039***	0.9103
Curved > straight	$\mathbf{3.55 \times 10^{-5}}$*	**0.0457**	0.1365	**0.0039***
Curved ≤ straight	~1	0.9543	0.8633	0.9961

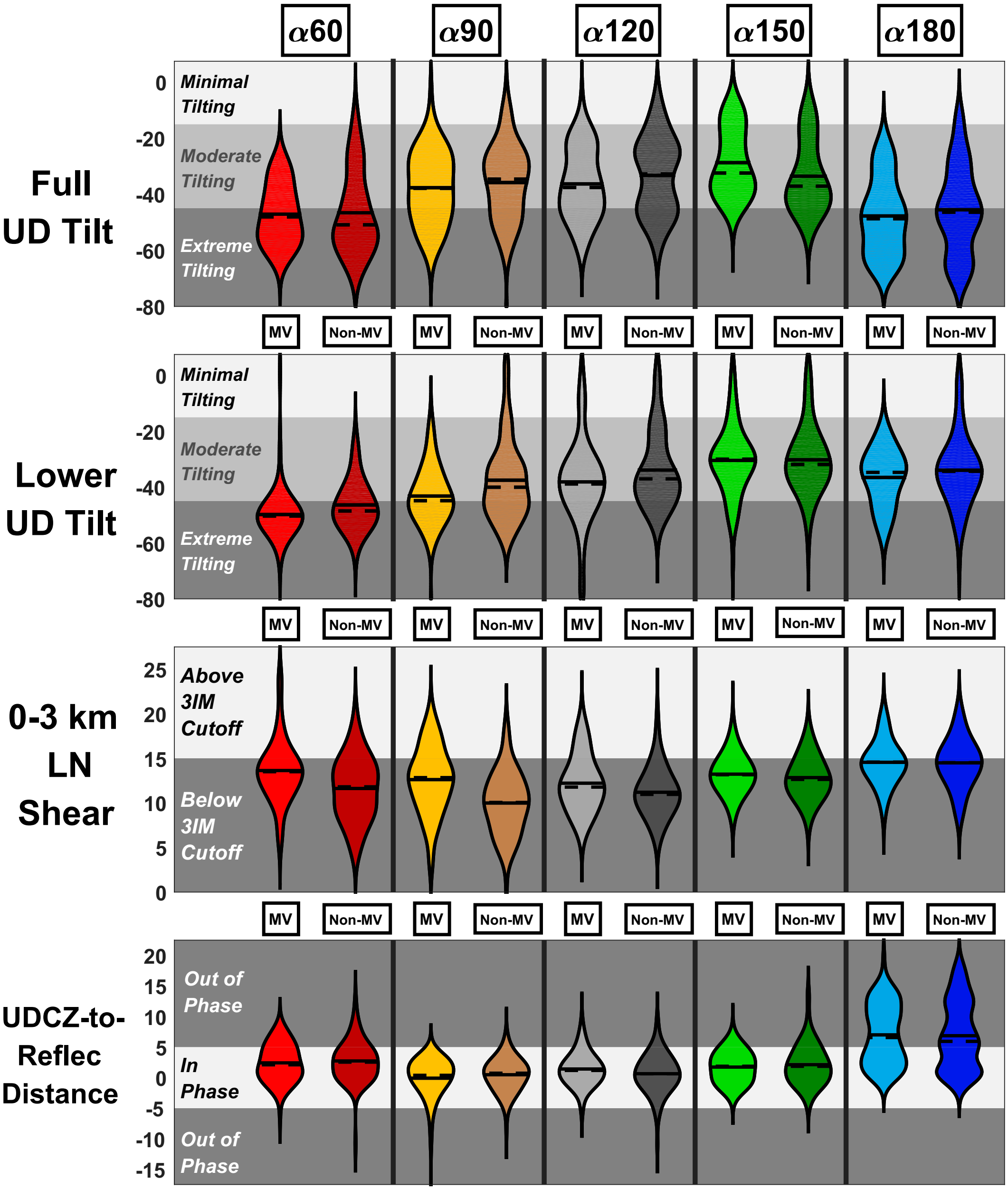

FIG. 13. Violin plots of full (0–10 km) and lower (0–2 km) updraft tilt (in degrees clockwise from vertical), LN shear ($\mathrm{m\ s^{-1}}$), and UDCZ-to-R distance (km) during hours 2–5, broken down by LL shear orientation. For each orientation, the left (lighter) plot represents variable distributions for MV segments, and the right (darker) plot corresponds to non-MV segments. The population mean (solid black line) and median (dashed black line) values are denoted. Also shown are variable-specific balance categories, sourced from 3IM, Ungar and Coniglio (2023), and this study.

4) Hodograph curvature (and similarly the presence of LL line-parallel shear) favors the production and maintenance of cyclonic rotation, in comparison to straight-line hodographs. There exists a critical value of LL line-parallel shear—roughly 7.5–10 $\mathrm{m\ s^{-1}}$—above which there is ample support for intense, long-lived cyclonic mesovortices.

Future QLCS modeling and observational work can further contextualize the presented results. The former would benefit from the added realism of incorporating frictional effects, other LL shear depths (e.g., deeper shear layers extending to 1 km AGL), and thermodynamic profiles spanning a broader CAPE spectrum. Furthermore, an assessment of the convective artifacts introduced by storm initialization [similar to the supercell sensitivity tests of Flournoy and Rasmussen (2023)] and other numerical modeling techniques are needed in order to develop more realistic methods for simulating squall lines [as in Labriola et al. (2023)]. Observationally, more comparisons

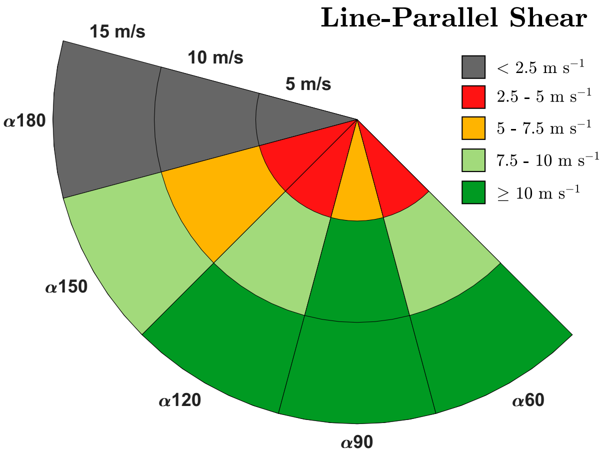

FIG. 14. Polar plots (as in Figs. 10–12) of LP shear corresponding to the base-state hodographs, color-coded by LP shear magnitude (m s^{-1}). LP shear categories (each exclusive, meaning that the upper bound is excluded) include <2.5 m s^{-1} (dark gray), 2.5–5 m s^{-1} (red), 5–7.5 m s^{-1} (gold), 7.5–10 m s^{-1} (light green), and ≥10 m s^{-1} (dark green).

between field measurements—such as those from the recent Propagation, Evolution and Rotation in Linear Storms (PERiLS; https://www.eol.ucar.edu/field_projects/perils) field campaign—and simulations of squall lines are crucial to understanding how QLCS cold pools and updrafts evolve in time to support intense low-level rotation.

In any case, our findings have major implications for both QLCS theory and forecasting. Physically, we have shown that alterations to shear over a relatively shallow layer can have far-reaching consequences for squall-line morphology, updraft intensity and rotation, and mesovortex production. While much of the QLCS literature has focused on LN shear impacts on system balance and mesovortexgenesis, we have demonstrated that LP shear plays a crucial role in fostering larger, more intense, and longer-lived cyclonic vortices—conceivably increasing the likelihood of QLCS tornadogenesis [as in Atkins et al. (2004)]. These factors, paired with questions about the ability of 3IM to describe system balance and its purported role in mesovortex formation, suggest that the current operational framework used for QLCS tornado prediction might benefit from a refocusing through the lens of this and other recent advances in QLCS science (e.g., Gibbs 2021; Goodnight et al. 2022; Ungar and Coniglio 2023).

A few missing pieces of this theoretical puzzle remain, however—namely, what storm-scale processes are contributing to changes in updraft and mesovortex character across the LL shear spectrum evaluated in our study? Furthermore, how do these changes affect the ability of LL QLCS updrafts to converge and rapidly intensify near-surface rotation? To this end, Part II will elucidate the underlying dynamics governing the different pathways by which these idealized squall lines generate and sustain mesovortices.

Acknowledgments. M. C. Brown and G. R. Marion were supported by the National Research Council Research Associateship Awards at the NOAA/National Severe Storms Laboratory. A Python package from Tim Supinie (https://github.com/tsupinie/wk-profiles) was used to develop the modulated Weisman–Klemp thermodynamic profiles used to initialize the simulations. Reviews from three anonymous reviewers strengthened the content and focus of this manuscript. The authors thank Pat Skinner and Thomas Galarneau for constructive comments during the preparation of this manuscript and George Bryan for his continued development and maintenance of CM1.

Data availability statement. All base-state soundings/hodographs and analysis scripts are archived locally and available upon request to the corresponding author.

APPENDIX

Three Ingredients Method (3IM) Calculations

a. 3IM ingredient 1: UDCZ-to-reflectivity distance

Following the methodology/discussion within this paper, storm OFBs (as estimated by the $\theta' = -1$ K contour) are used as a proxy for the UDCZ. The leading reflectivity gradient is approximated using the easternmost extent of the 45-dBZ contour (averaged in the 0–500-m layer). This is slightly lower than the 50-dBZ threshold utilized in Ungar and Coniglio (2023) but showed the best agreement with the leading edge of storm reflectivity objects. The distance between these two boundaries constitutes our UDCZ-to-reflectivity (UDCZ-to-R) distance. Following the sign convention of Ungar and Coniglio (2023), positive values imply an OFB boundary that leads our convection (i.e., outflow-dominant system), and neutral/positive values imply closer phasing between these storm attributes.

b. 3IM ingredient 2: line-normal shear calculations

A 20-km moving window running north–south (N–S) along each identified OFB is used to generate a linear least squares fit line (with associated OFB points) and calculate the OFB angle. Other window widths were tested—20 km was sufficient to resolve smaller-scale variations in OFB angle (similar to the 15-km segment implemented in Ungar and Coniglio 2023) while retaining broader-scale orientation in areas of complex OFB geometry (e.g., inflection points and areas of substantial deformation). Storm-relative winds in an area 5–25 km east of the OFB are gathered and projected onto the local OFB angle to calculate line-normal and line-parallel SR flow components within the associated QLCS segment.

c. 3IM ingredient 3: bowing segment identification

Ingredient 2 calculations result in a continuous array of OFB angles at each model time output. Identification of QLCS bowing segments is accomplished by applying an algorithm which combines OFB angle thresholds (e.g., minimum deviation of OFB from N–S orientation) to identify the start/end points of bowing segments. In other words, when a given

OFB rotates sufficiently clockwise (from N–S orientation) and then back counterclockwise, we infer the presence of a local surge. The zero crossing of this transition is used to denote bowing apexes. If multiple apexes are identified, the one associated with the largest zonal excursion from the system-averaged OFB position is retained. Several deviation angle thresholds were tested for completeness, and 15° was found to consistently identify a wide range of bowing segment sizes, without flagging small and/or transient OFB inflections.

REFERENCES

Alfaro, D. A., 2017: Low-tropospheric shear in the structure of squall lines: Impacts on latent heating under layer-lifting ascent. *J. Atmos. Sci.*, **74**, 229–248, https://doi.org/10.1175/JAS-D-16-0168.1.

——, and M. Khairoutdinov, 2015: Thermodynamic constraints on the morphology of simulated midlatitude squall lines. *J. Atmos. Sci.*, **72**, 3116–3137, https://doi.org/10.1175/JAS-D-14-0295.1.

Atkins, N. T., and M. St. Laurent, 2009a: Bow echo mesovortices. Part I: Processes that influence their damaging potential. *Mon. Wea. Rev.*, **137**, 1497–1513, https://doi.org/10.1175/2008MWR2649.1.

——, and ——, 2009b: Bow echo mesovortices. Part II: Their genesis. *Mon. Wea. Rev.*, **137**, 1514–1532, https://doi.org/10.1175/2008MWR2650.1.

——, J. M. Arnott, R. W. Przybylinski, R. A. Wolf, and B. D. Ketcham, 2004: Vortex structure and evolution within bow echoes. Part I: Single-Doppler and damage analysis of the 29 June 1998 derecho. *Mon. Wea. Rev.*, **132**, 2224–2242, https://doi.org/10.1175/1520-0493(2004)132<2224:VSAEWB>2.0.CO;2.

——, C. S. Bouchard, R. W. Przybylinski, R. J. Trapp, and G. Schmocker, 2005: Damaging surface wind mechanisms within the 10 June 2003 Saint Louis bow echo during BAMEX. *Mon. Wea. Rev.*, **133**, 2275–2296, https://doi.org/10.1175/MWR2973.1.

Boyer, C. H., and J. M. L. Dahl, 2020: The mechanisms responsible for large near-surface vertical vorticity within simulated supercells and quasi-linear storms. *Mon. Wea. Rev.*, **148**, 4281–4297, https://doi.org/10.1175/MWR-D-20-0082.1.

Brown, M. C., and C. J. Nowotarski, 2019: The influence of lifting condensation level on low-level outflow and rotation in simulated supercell thunderstorms. *J. Atmos. Sci.*, **76**, 1349–1372, https://doi.org/10.1175/JAS-D-18-0216.1.

Bryan, G. H., and J. M. Fritsch, 2002: A benchmark simulation for moist nonhydrostatic numerical models. *Mon. Wea. Rev.*, **130**, 2917–2928, https://doi.org/10.1175/1520-0493(2002)130<2917:ABSFMN>2.0.CO;2.

Burgess, D. W., and B. F. Smull, 1990: Doppler radar observations of a bow echo associated with a long-track severe windstorm. Preprints, *16th Conf. on Severe Local Storms*, Kananaskis Park, Alberta, Canada, Amer. Meteor. Soc., 203–208.

Coffer, B. E., and M. D. Parker, 2015: Impacts of increasing low-level shear on supercells during the early evening transition. *Mon. Wea. Rev.*, **143**, 1945–1969, https://doi.org/10.1175/MWR-D-14-00328.1.

Cohen, A. E., M. C. Coniglio, S. F. Corfidi, and S. J. Corfidi, 2007: Discrimination of mesoscale convective system environments using sounding observations. *Wea. Forecasting*, **22**, 1045–1062, https://doi.org/10.1175/WAF1040.1.

Coniglio, M. C., S. F. Corfidi, and J. S. Kain, 2012: Views on applying RKW theory: An illustration using the 8 May 2009 derecho-producing convective system. *Mon. Wea. Rev.*, **140**, 1023–1043, https://doi.org/10.1175/MWR-D-11-00026.1.

Davies-Jones, R., 1984: Streamwise vorticity: The origin of updraft rotation in supercell storms. *J. Atmos. Sci.*, **41**, 2991–3006, https://doi.org/10.1175/1520-0469(1984)041<2991:SVTOOU>2.0.CO;2.

Deardorff, J. W., 1980: Stratocumulus-capped mixed layers derived from a three-dimensional model. *Bound.-Layer Meteor.*, **18**, 495–527, https://doi.org/10.1007/BF00119502.

Evans, J. S., and C. A. Doswell III, 2001: Examination of derecho environments using proximity soundings. *Wea. Forecasting*, **16**, 329–342, https://doi.org/10.1175/1520-0434(2001)016<0329:EODEUP>2.0.CO;2.

Flournoy, M. D., and M. C. Coniglio, 2019: Origins of vorticity in a simulated tornadic mesovortex observed during PECAN on 6 July 2015. *Mon. Wea. Rev.*, **147**, 107–134, https://doi.org/10.1175/MWR-D-18-0221.1.

——, and E. N. Rasmussen, 2023: The influence of convection initiation strength on subsequent simulated supercell evolution. *Mon. Wea. Rev.*, **151**, 2179–2203, https://doi.org/10.1175/MWR-D-22-0069.1.

Funk, T. W., K. E. Darmofal, J. D. Kirkpatrick, V. DeWald, R. W. Przybylinski, G. K. Schmocker, and Y.-J. Lin, 1999: Storm reflectivity and mesocyclone evolution associated with the 15 April 1994 squall line over Kentucky and southern Indiana. *Wea. Forecasting*, **14**, 976–993, https://doi.org/10.1175/1520-0434(1999)014<0976:SRAMEA>2.0.CO;2.

Gibbs, J. G., 2021: Evaluating precursor signals for QLCS tornado and higher impact straight-line wind events. *J. Oper. Meteor.*, **9**, 62–75, https://doi.org/10.15191/nwajom.2021.0905.

Goodnight, J. S., D. A. Chehak, and R. J. Trapp, 2022: Quantification of QLCS tornadogenesis, associated characteristics, and environments across a large sample. *Wea. Forecasting*, **37**, 2087–2105, https://doi.org/10.1175/WAF-D-22-0016.1.

Guarriello, F., C. J. Nowotarski, and C. C. Epifanio, 2018: Effects of the low-level wind profile on outflow position and near-surface vertical vorticity in simulated supercell thunderstorms. *J. Atmos. Sci.*, **75**, 731–753, https://doi.org/10.1175/JAS-D-17-0174.1.

Hane, C. E., 1973: The squall line thunderstorm: Numerical experimentation. *J. Atmos. Sci.*, **30**, 1672–1690, https://doi.org/10.1175/1520-0469(1973)030<1672:TSLTNE>2.0.CO;2.

Labriola, J. D., J. A. Gibbs, and L. J. Wicker, 2023: A method for generating a quasi-linear convective system suitable for observing system simulation experiments. *Geosci. Model Dev.*, **16**, 1779–1799, https://doi.org/10.5194/gmd-16-1779-2023.

Latimer, S., and A. Kula, 2010: A comparison of warm and cool season tornadic quasi-linear convective systems in North Alabama. Preprints, *26th Conf. on Interactive Information and Processing Systems (IIPS) for Meteorology, Oceanography and Hydrology*, Atlanta, GA, Amer. Meteor. Soc., 11B.6, https://ams.confex.com/ams/pdfpapers/158140.pdf.

Lee, B. D., and R. B. Wilhelmson, 1997: The numerical simulation of nonsupercell tornadogenesis. Part II: Evolution of a family of tornadoes along a weak outflow boundary. *J. Atmos. Sci.*, **54**, 2387–2415, https://doi.org/10.1175/1520-0469(1997)054<2387:TNSONT>2.0.CO;2.

——, and ——, 2000: The numerical simulation of nonsupercell tornadogenesis. Part III: Parameter tests investigating the role of CAPE, vortex sheet strength, and boundary layer vertical shear. *J. Atmos. Sci.*, **57**, 2246–2261, https://doi.org/10.1175/1520-0469(2000)057<2246:TNSONT>2.0.CO;2.

Li, Z., P. Zuidema, P. Zhu, and H. Morrison, 2015: The sensitivity of simulated shallow cumulus convection and cold pools to microphysics. *J. Atmos. Sci.*, **72**, 3340–3355, https://doi.org/10.1175/JAS-D-14-0099.1.

Lovell, L. T., and M. D. Parker, 2022: Simulated QLCS vortices in a high-shear, low-CAPE environment. *Wea. Forecasting*, **37**, 989–1012, https://doi.org/10.1175/WAF-D-21-0133.1.

Lyza, A. W., A. W. Clayton, K. R. Knupp, E. Lenning, M. T. Friedlein, R. L. Castro, and E. S. Bentley, 2017: Analysis of mesovortex characteristics, behavior, and interactions during the second 30 June–1 July 2014 midwestern derecho event. *Electron. J. Severe Storms Meteor.*, **12** (2), https://atlas.niu.edu/klot/lot2/Media/events/studies/EJSSM-Summer2017.pdf.

Mansell, E. R., C. L. Ziegler, and E. C. Bruning, 2010: Simulated electrification of a small thunderstorm with two-moment bulk microphysics. *J. Atmos. Sci.*, **67**, 171–194, https://doi.org/10.1175/2009JAS2965.1.

Marion, G. R., and R. J. Trapp, 2019: The dynamical coupling of convective updrafts, downdrafts, and cold pools in simulated supercell thunderstorms. *J. Geophys. Res. Atmos.*, **124**, 664–683, https://doi.org/10.1029/2018JD029055.

——, and ——, 2021: Controls of quasi-linear convective system tornado intensity. *J. Atmos. Sci.*, **78**, 1189–1205, https://doi.org/10.1175/JAS-D-20-0164.1.

Markowski, P. M., and Y. P. Richardson, 2014: The influence of environmental low-level shear and cold pools on tornadogenesis: Insights from idealized simulations. *J. Atmos. Sci.*, **71**, 243–275, https://doi.org/10.1175/JAS-D-13-0159.1.

——, and G. H. Bryan, 2016: LES of laminar flow in the PBL: A potential problem for convective storm simulations. *Mon. Wea. Rev.*, **144**, 1841–1850, https://doi.org/10.1175/MWR-D-15-0439.1.

Morrison, H., and J. Milbrandt, 2011: Comparison of two-moment bulk microphysics schemes in idealized supercell thunderstorm simulations. *Mon. Wea. Rev.*, **139**, 1103–1130, https://doi.org/10.1175/2010MWR3433.1.

——, J. A. Curry, and V. I. Khvorostyanov, 2005: A new double-moment microphysics parameterization for application in cloud and climate models. Part I: Description. *J. Atmos. Sci.*, **62**, 1665–1677, https://doi.org/10.1175/JAS3446.1.

Mulholland, J. P., J. M. Peters, and H. Morrison, 2021: How does vertical wind shear influence entrainment in squall lines? *J. Atmos. Sci.*, **78**, 1931–1946, https://doi.org/10.1175/JAS-D-20-0299.1.

Murdzek, S. S., Y. P. Richardson, P. M. Markowski, and M. R. Kumjian, 2022: How the environmental lifting condensation level affects the sensitivity of simulated convective storm cold pools to the microphysics parameterization. *Mon. Wea. Rev.*, **150**, 2527–2552, https://doi.org/10.1175/MWR-D-21-0258.1.

Murphy, T. A., T. M. Stetzer, L. Walker, T. Fricker, B. Bryant, and C. Woodrum, 2022: Analysis of the 12 April 2020 northern Louisiana tornadic QLCS. *J. Oper. Meteor.*, **10**, 43–62, https://doi.org/10.15191/nwajom.2022.1004.

Nolen, R. H., 1959: A radar pattern associated with tornadoes. *Bull. Amer. Meteor. Soc.*, **40**, 277–279, https://doi.org/10.1175/1520-0477-40.6.277.

Okubo, A., 1970: Horizontal dispersion of floatable particles in the vicinity of velocity singularities such as convergences. *Deep-Sea Res. Oceanogr. Abstr.*, **17**, 445–454, https://doi.org/10.1016/0011-7471(70)90059-8.

Parker, M. D., 2010: Relationship between system slope and updraft intensity in squall lines. *Mon. Wea. Rev.*, **138**, 3572–3578, https://doi.org/10.1175/2010MWR3441.1.

Peters, J. M., C. J. Nowotarski, and H. Morrison, 2019: The role of vertical wind shear in modulating maximum supercell updraft velocities. *J. Atmos. Sci.*, **76**, 3169–3189, https://doi.org/10.1175/JAS-D-19-0096.1.

——, ——, J. P. Mulholland, and R. L. Thompson, 2020: The influences of effective inflow layer streamwise vorticity and storm-relative flow on supercell updraft properties. *J. Atmos. Sci.*, **77**, 3033–3057, https://doi.org/10.1175/JAS-D-19-0355.1.

Przybylinski, R. W., 1995: The bow echo: Observations, numerical simulations, and severe weather detection methods. *Wea. Forecasting*, **10**, 203–218, https://doi.org/10.1175/1520-0434(1995)010<0203:TBEONS>2.0.CO;2.

Rotunno, R., J. B. Klemp, and M. L. Weisman, 1988: A theory for strong, long-lived squall lines. *J. Atmos. Sci.*, **45**, 463–485, https://doi.org/10.1175/1520-0469(1988)045<0463:ATFSLL>2.0.CO;2.

Schaumann, J. S., and R. W. Przybylinski, 2012: Operational application of 0–3 km bulk shear vectors in assessing quasi-linear convective system mesovortex and tornado potential. *26th Conf. on Severe Local Storms*, Nashville, TN, Amer. Meteor. Soc., P9.10, https://ams.confex.com/ams/26SLS/webprogram/Manuscript/Paper212008/SchaumannSLS2012_P142.pdf.

Schenkman, A. D., M. Xue, and A. Shapiro, 2012: Tornadogenesis in a simulated mesovortex within a mesoscale convective system. *J. Atmos. Sci.*, **69**, 3372–3390, https://doi.org/10.1175/JAS-D-12-038.1.

Smull, B. F., and R. A. Houze Jr., 1987: Rear inflow in squall lines with trailing stratiform precipitation. *Mon. Wea. Rev.*, **115**, 2869–2889, https://doi.org/10.1175/1520-0493(1987)115<2869:RIISLW>2.0.CO;2.

Stensrud, D. J., M. C. Coniglio, R. P. Davies-Jones, and J. S. Evans, 2005: Comments on "'A theory for strong long-lived squall lines' revisited". *J. Atmos. Sci.*, **62**, 2989–2996, https://doi.org/10.1175/JAS3514.1.

Thompson, R. L., B. T. Smith, J. S. Grams, A. R. Dean, and C. Broyles, 2012: Convective modes for significant severe thunderstorms in the contiguous United States. Part II: Supercell and QLCS tornado environments. *Wea. Forecasting*, **27**, 1136–1154, https://doi.org/10.1175/WAF-D-11-00116.1.

Thorpe, A. J., M. J. Miller, and M. W. Moncrieff, 1982: Two-dimensional convection in non-constant shear: A model of mid-latitude squall lines. *Quart. J. Roy. Meteor. Soc.*, **108**, 739–762, https://doi.org/10.1002/qj.49710845802.

Trapp, R. J., and M. L. Weisman, 2003: Low-level mesovortices within squall lines and bow echoes. Part II: Their genesis and implications. *Mon. Wea. Rev.*, **131**, 2804–2823, https://doi.org/10.1175/1520-0493(2003)131<2804:LMWSLA>2.0.CO;2.

Ungar, M. D., and M. C. Coniglio, 2023: Using radiosonde observations to assess the "Three Ingredients Method" to forecast QLCS mesovortices. *Wea. Forecasting*, **38**, 2441–2460, https://doi.org/10.1175/WAF-D-22-0176.1.

Wade, A. R., and M. D. Parker, 2021: Dynamics of simulated high-shear, low-CAPE supercells. *J. Atmos. Sci.*, **78**, 1389–1410, https://doi.org/10.1175/JAS-D-20-0117.1.

Weiner, A., 2022: Case study of the extreme high-shear/low-CAPE, strongly-forced Tennessee Valley QLCS of 12 February 2020. M.S. thesis, Dept. of Atmospheric and Earth Science, University of Alabama in Huntsville, 152 pp., https://louis.uah.edu/uah-theses/387/.

Weisman, M. L., and J. B. Klemp, 1982: The dependence of numerically simulated convective storms on vertical wind shear and buoyancy. *Mon. Wea. Rev.*, **110**, 504–520, https://doi.org/10.1175/1520-0493(1982)110<0504:TDONSC>2.0.CO;2.

——, and ——, 1984: The structure and classification of numerically simulated convective storms in directionally varying wind shears. *Mon. Wea. Rev.*, **112**, 2479–2498, https://doi.org/10.1175/1520-0493(1984)112<2479:TSACON>2.0.CO;2.

——, and R. J. Trapp, 2003: Low-level mesovortices within squall lines and bow echoes. Part I: Overview and dependence on environmental shear. *Mon. Wea. Rev.*, **131**, 2779–2803, https://doi.org/10.1175/1520-0493(2003)131<2779:LMWSLA>2.0.CO;2.

——, and R. Rotunno, 2004: "A theory for strong long-lived squall lines" revisited. *J. Atmos. Sci.*, **61**, 361–382, https://doi.org/10.1175/1520-0469(2004)061<0361:ATFSLS>2.0.CO;2.

——, J. B. Klemp, and R. Rotunno, 1988: Structure and evolution of numerically simulated squall lines. *J. Atmos. Sci.*, **45**, 1990–2013, https://doi.org/10.1175/1520-0469(1988)045<1990:SAEONS>2.0.CO;2.

Weiss, J., 1991: The dynamics of enstrophy transfer in two-dimensional hydrodynamics. *Physica D*, **48**, 273–294, https://doi.org/10.1016/0167-2789(91)90088-Q.

Wicker, L. J., 1996: The role of near surface wind shear on low-level mesocyclone generation and tornadoes. Preprints, *18th Conf. on Severe Local Storms*, San Francisco, CA, Amer. Meteor. Soc., 115–119.

Wilks, D. S., 2011: *Statistical Methods in the Atmospheric Sciences*. 3rd ed. Elsevier, 676 pp.

Williams, B. M., J. S. Allen, and J. W. Zeitler, 2018: Anticipating QLCS tornadogenesis for decision support: The three-ingredient method during the 19–20 February 2017 south-central Texas tornadic QLCS event. *98th American Meteorological Society Annual Meeting*, Austin, TX, Amer. Meteor. Soc., 22 pp., https://ams.confex.com/ams/98Annual/webprogram/Paper331351.html.

Xu, Q., 1992: Density currents in shear flows-a two-fluid model. *J. Atmos. Sci.*, **49**, 511–524, https://doi.org/10.1175/1520-0469(1992)049<0511:DCISFA>2.0.CO;2.

Xu, X., M. Xue, and Y. Wang, 2015: The genesis of mesovortices within a real-data simulation of a bow echo system. *J. Atmos. Sci.*, **72**, 1963–1986, https://doi.org/10.1175/JAS-D-14-0209.1.